Chromatin compartment dynamics

in a haploinsufficient model of cardiac laminopathy

Alessandro Bertero[1,2,3], Paul A. Fields[1,2,3], Alec S. T. Smith[2,3,4], Andrea Leonard[2,3,5], Kevin Beussman[2,3,5], Nathan J. Sniadecki[2,3,4,5], Deok-Ho Kim[2,3,4], Hung-Fat Tse[6], Lil Pabon[1,2,3], Jay Shendure[7,8], William S. Noble[7], and Charles E. Murry[1,2,3,4,9]

[1] Department of Pathology, University of Washington, Seattle, WA, USA

[2] Center for Cardiovascular Biology, University of Washington, Seattle, WA, USA

[3] Institute for Stem Cell and Regenerative Medicine, University of Washington, Seattle, WA, USA

[4] Department of Bioengineering, University of Washington, Seattle, WA, USA

[5] Department of Mechanical Engineering, University of Washington, Seattle, WA, USA

[6] Cardiology Division, Department of Medicine, The University of Hong Kong, Hong Kong, China

[7] Department of Genome Sciences, University of Washington, Seattle, Washington, USA

[8] Howard Hughes Medical Institute, Seattle, Washington, USA

[9] Department of Medicine/Cardiology, University of Washington, Seattle, WA, USA

For correspondence pertaining to this article, contact:

Charles E. Murry, MD, PhD
University of Washington
850 Republican Street
Brotman Building Room 453
Seattle, WA 98109
206-616-8685
murry@uw.edu
ORCID: 0000-0003-3862-6773

Abstract

Pathogenic mutations in A-type nuclear lamins cause dilated cardiomyopathy, which is postulated to result from dysregulated gene expression due to changes in chromatin organization into active and inactive compartments. To test this, we performed genome-wide chromosome conformation analyses (Hi-C) in human induced pluripotent stem cell-derived cardiomyocytes (hiPSC-CMs) with a haploinsufficient mutation for lamin A/C. Compared to gene-corrected cells, mutant hiPSC-CMs have marked electrophysiological and contractile alterations, with modest gene expression changes. While large-scale changes in chromosomal topology are evident, differences in chromatin compartmentalization are limited to a few hotspots that escape inactivation during cardiogenesis. These regions exhibit upregulation of multiple non-cardiac genes including *CACNA1A*, encoding for neuronal P/Q-type calcium channels. Pharmacological inhibition of the resulting current partially mitigates the electrical alterations. On the other hand, A/B compartment changes do not explain most gene expression alterations in mutant hiPSC-CMs. We conclude that global errors in chromosomal compartmentation are not the primary pathogenic mechanism in heart failure due to lamin A/C haploinsufficiency.

Summary

Bertero et al. observe that lamin A/C haploinsufficiency in human cardiomyocytes markedly alters electrophysiology, contractility, gene expression, and chromosomal topology. Contrary to expectations, however, changes in chromatin compartments involve just few regions, and most dysregulated genes lie outside these hotspots.

Condensed title

Genomic effects of lamin A/C haploinsufficiency

2

Introduction

Chromatin organization in the three-dimensional space has emerged as a key layer of mammalian gene expression control. The development of powerful technologies to map chromatin architecture, in particular genome-wide chromosome conformation capture (Hi-C; Lieberman-Aiden et al., 2009), has revealed that such 3D structure is complex, non-random, and hierarchical (Yu and Ren, 2017). Short- and long-range intra-chromosomal (*cis*) DNA interactions are generally constrained within topologically associating domains (TADs; Dixon et al., 2012; Nora et al., 2012; Sexton et al., 2012). TADs tend to interact based on their epigenetic status and transcriptional activity, thus dividing chromosomes into two types of large-scale compartments generally called active and inactive (A and B, respectively; Simonis et al., 2006; Lieberman-Aiden et al., 2009; Rao et al., 2014). Inter-chromosomal (*trans*) interactions predominantly involve the A compartment and are generally more limited, as chromosomes occupy distinct nuclear territories (Bolzer et al., 2005; Branco and Pombo, 2006; Kalhor et al., 2012).

Moving beyond the third dimension, there has been growing interest in understanding the functional changes in chromatin organization during development and in disease (Dekker et al., 2017). An emerging body of work has shown that TADs are largely invariant across cell types (Dixon et al., 2012, 2015; Fraser et al., 2015; Won et al., 2016; Schmitt et al., 2016; Fields et al., 2017). On the other hand, these same studies have established that pluripotent stem cell differentiation leads to a substantial degree of A/B compartment reorganization (e.g. ~20% of the genome), and that this is associated with important developmental changes in gene expression. Nevertheless, the precise mechanisms that regulate chromatin compartmentalization dynamics during development are still poorly understood (Adriaens et al., 2018). In the context of disease, disruption of TADs due to copy number variations or point mutations was shown to lead to congenital developmental disorders and cancers (Lupiáñez et al., 2015; Katainen et al., 2015; Redin et al., 2017; Sun et al., 2018). In contrast, whether dysregulation of A/B compartments plays a role in functional changes of gene expression leading to human disease is still unclear (Krumm and Duan, 2018).

The nuclear lamina has been proposed as a regulator of chromatin compartmentalization in development and disease (Buchwalter et al., 2018). The lamina lies along the inner nuclear membrane and is a complex mesh of nuclear intermediate filaments (A- and B-type lamins) and lamin-associated proteins. This structure provides key mechanical support to the nucleus, and is an important hub for the control of intracellular signaling (Dobrzynska et al., 2016). Moreover, the nuclear lamina interacts with large chromatin regions, aptly named lamin-associated domains (LADs; van Steensel and Belmont, 2017),

3

80   which show heterochromatic features such as low gene density, enrichment for repressive histone marks,
81   and poor transcriptional activity (Guelen et al., 2008). Several studies have established that such
82   peripherally-located LADs strongly correlate with the B compartment, while the A compartment is
83   predominantly in the nuclear interior (Kind et al., 2015; Stevens et al., 2017; Luperchio et al., 2017; Zheng
84   et al., 2018). Both lamins and lamin-associated proteins, such as LBR (lamin B receptor), can directly
85   interact with chromatin (Yuan et al., 1991; Taniura et al., 1995; Ye and Worman, 1994, 1996). Based on
86   this and on the results of loss-of-function studies it has been proposed that the nuclear lamina tethers
87   LADs at the nuclear periphery (Solovei et al., 2013; Harr et al., 2015; Luperchio et al., 2017). However,
88   the precise role of A- and B-type lamins in chromatin compartmentalization is still being debated
89   (Amendola and van Steensel, 2015; Zheng et al., 2015, 2018; Adriaens et al., 2018).

90

91   Elucidating the function of A-type lamins (lamin A and lamin C, which result from alternative splicing of
92   the *LMNA* gene) is particularly important not only from a cell and developmental biology perspective, but
93   also because of their involvement in human disease. *LMNA* mutations lead to a wide spectrum of
94   conditions collectively referred to as laminopathies (Capell and Collins, 2006). Notably, nearly 80% of all
95   reported *LMNA* mutations lead to isolated striated muscle disease, with another 10% leading to
96   overlapping phenotypes that also affect striated muscles (Bertrand et al., 2011). The majority of patients
97   with striated muscle laminopathies develop dilated cardiomyopathy (DCM), with variable skeletal muscle
98   manifestations (Captur et al., 2018). Mutations in *LMNA* are generally considered the second-most most
99   common cause of familial DCM, depending on the ethnicity of the population (Akinrinade et al., 2015;
100   Haas et al., 2015; Tobita et al., 2018). Compared to other types of DCM, *LMNA*-DCM is quite atypical as
101   it is characterized by early onset of life-threatening cardiac electrical abnormalities such as severe
102   conduction system disease and/or atrial and ventricular arrhythmias (Van Rijsingen et al., 2012;
103   Hasselberg et al., 2018; Kumar et al., 2016). Another peculiar aspect of *LMNA*-DCM is that not all patients
104   go on to develop left ventricular dilatation and reduced contractile function, which are typical hallmarks
105   of DCM (Van Berlo et al., 2005; Kumar et al., 2016; Tobita et al., 2018). Nevertheless, patients with
106   *LMNA*-DCM are poorly responsive to medical treatments and show minimal beneficial left ventricular
107   reverse remodeling (Tobita et al., 2018). This may be explained by the higher incidence of cardiac fibrosis
108   in *LMNA*-DCM patients (van Tintelen et al., 2007b; Fontana et al., 2013; Tobita et al., 2018). Overall,
109   *LMNA*-DCM (which throughout the rest of the manuscript we will refer to as "cardiac laminopathy") is a
110   more severe disease compared to other genetic DCM, with young onset, high penetrance, poor
111   prognosis, and frequent need for heart transplantation as the only current available therapy (Hasselberg
112   et al., 2018; Tobita et al., 2018).

113

114 Over the nearly 20 years since the first report linking mutations in *LMNA* to human disease (Bonne et al.,
115 1999), three central non-mutually exclusive mechanisms have been hypothesized to underpin the
116 pathogenesis of cardiac laminopathy: (1) impaired nuclear mechanoresistance *via* the nucleo-
117 cytoplasmic network, or "mechanical hypothesis"; (2) alteration of lamin A/C-controlled intracellular
118 signaling pathways, or "signaling hypothesis"; and (3) dysregulation of heterochromatin organization
119 leading to gene expression alterations, or "chromatin hypothesis" (Worman and Courvalin, 2004; Cattin
120 et al., 2013). While evidence supporting the first two hypotheses has accumulated over the years, and
121 therapies targeting intracellular signaling alterations are being pre-clinically developed (Cattin et al., 2013;
122 Captur et al., 2018), the possible involvement of chromatin dysregulation in cardiac laminopathy is still
123 far from established (Adriaens et al., 2018). Indeed, while there have been reports of changes in the
124 nuclear positioning of selected loci in patients with cardiac laminopathy (Meaburn et al., 2007; Mewborn
125 et al., 2010), the functional consequences of such alterations on the disease pathogenesis are unclear.
126 Moreover, these studies have relied on fibroblasts instead of cardiomyocytes, the primary cell type
127 involved in cardiac laminopathy. Most importantly, to the best of our knowledge the 3D chromatin
128 organization changes associated with cardiac laminopathy have not yet, been tested at a genome-wide
129 level.

130

131 To address these limitations, we performed genome-wide chromosome conformation capture (Hi-C) and
132 gene expression (RNA-seq) analyses to examine the changes in 3D chromatin architecture induced by
133 a haploinsufficient *LMNA* mutation in cardiomyocytes derived from human induced pluripotent stem cells
134 (hiPSC-CMs). We hypothesized that decreased expression of A-type lamins would lead to broad
135 functional alterations in A/B compartmentalization leading to aberrant gene expression. We observed
136 that mutant hiPSC-CMs show marked alterations in their electrophysiological and contractile phenotypes,
137 broad dysregulation of gene expression, and alterations in large-scale chromosomal topology
138 (strengthened separation between chromosome territories and between chromatin compartments).
139 However, functional changes in A/B compartmentalization are limited to a few genomic hotspots that
140 normally transition from the A to B compartment during cardiogenesis, but remain in A in lamin A/C
141 haploinsufficient hiPSC-CMs. These hotspots exhibit upregulation of multiple non-cardiac genes,
142 including the neuronal gene *CACNA1A*, which encodes for P/Q-type calcium channels. Of note, however,
143 changes in A/B compartments do not explain the majority of gene expression changes, including the
144 upregulation of the cardiac gene *CACNA1C*, which encodes for the L-type calcium channel.
145 Pharmacological inhibition of P/Q-type calcium currents partially mitigates the field potential duration
146 elongation observed in mutant hiPSC-CMs, while inhibition of L-type calcium currents has a more
147 powerful effect. We conclude that, while *LMNA* haploinsufficient mutations functionally affect selected

5

148   aspects of 3D chromatin organization in human cardiomyocytes, altered A/B compartmentalization does

149   not represent the primary mechanism directly leading to gene expression changes and disease

150   pathogenesis.

151

152   **Results**

153

154   **Generation of an *in vitro* model of cardiac lamin A/C haploinsufficiency**

155   To investigate the role of chromatin dynamics in cardiac laminopathy, we took advantage of hiPSCs

156   bearing a heterozygous nonsense mutation in *LMNA* predicted to cause premature truncation of both

157   lamin A and lamin C splicing isoforms (c.672C>T, resulting in p.Arg225*, which we will refer to as R225X;

158   Fig. 1A). This hiPSC line was previously derived from a 56-year-old male patient who developed severe

159   cardiac conduction disease evolving into heart failure, a condition that segregated within the family with

160   autosomal dominant inheritance of the R225X mutation (Siu et al., 2012). This same mutation has been

161   reported in multiple other cohorts with similar symptoms (van Tintelen et al., 2007a; Saga et al., 2009;

162   Jakobs et al., 2001), establishing it as a *bona fide* genetic cause of cardiac laminopathy.

163

164   It is well established that variability among hiPSC lines can profoundly influence both molecular and

165   cellular phenotypes (Ortmann and Vallier, 2017), which is particularly evident when assessing the

166   complex electrophysiology and contractile properties of hiPSC-CMs (Sala et al., 2017). Thus, we decided

167   to generate isogenic control hiPSCs by correcting the R225X mutation back to the wild-type allele, a

168   strategy currently considered the gold standard to determine the association between genotype and

169   phenotype in hiPSC-CMs (Bellin et al., 2013; Kodo et al., 2016; Mosqueira et al., 2018). By leveraging

170   existing methods (Yusa, 2013), we designed a two-step scarless gene editing strategy relying on

171   CRISPR/Cas9-facilitated homologous recombination of a targeting vector containing the wild-type allele

172   in the 3' homology arm, and an excisable piggyBac drug resistance cassette (Fig. S1A-B). To control for

173   the potential variability between hiPSC sublines, we obtained two isogenic control hiPSCs using distinct

174   sgRNA sequences (Fig. 1B and S1C-D). The resulting hiPSCs, which we will refer to as Corr.1 and Corr.2

175   (short for Corrected 1 and Corrected 2) were karyotypically normal (Fig. S1E).

176

177   Lamin A/C is expressed at very low levels in human pluripotent stem cells, and is upregulated during

178   differentiation (Constantinescu et al., 2006; Liu et al., 2011). Given that hiPSC-CMs are quite immature

179   (Yang et al., 2014), we sought to first confirm whether hiPSC-CMs express substantial levels of lamin

180   A/C. Further, we tested the consequence of the R225X mutation on lamin A/C expression at the transcript

181   and protein level. For this, we differentiated hiPSCs into hiPSC-CMs using an established protocol based

6

182 on the temporal modulation of WNT signaling using small molecules (Burridge et al., 2014; Fields et al.,

183 2017; Fig. 1C). Both mutant and corrected hiPSCs could be differentiated with high efficiency, as

184 measured by flow-cytometry for TNNT2 (Fig. 1D, Video S1, and Video S2; 91.6% ± 3.2%, 94.4% ± 2.5%,

185 and 91.3% ± 3.1% for Mutant, Corr.1, and Corr.2, respectively; average ± SEM of n = 4 independent

186 differentiations). Western blot and quantitative reverse transcription PCR (RT-qPCR) confirmed that all

187 hiPSC lines underwent the expected developmental progression through mesoderm and cardiac

188 progenitors before reaching a cardiomyocyte phenotype (Fig. 1F and S2A). Lamin A/C was upregulated

189 specifically in hiPSC-CMs, and mutant lines showed significantly reduced levels of both mRNA and

190 protein compared to both corrected controls (Fig. 1E-G). Of note, no detectable protein truncation was

191 detected by western blot (Fig. S2B), and lamin A/C expression in mutant hiPSC-CMs also proved to be

192 reduced when compared to cardiomyocytes generated from an unrelated hiPSC line derived from a

193 healthy individual (Fig. S2C). Finally, other minor *LMNA* isoforms were undetectable or nearly

194 undetectable by RT-qPCR in both control and mutant hiPSC-CMs, excluding possible compensatory

195 mechanisms (data not shown). These gene expression data agree with earlier findings from analysis of

196 skin fibroblasts bearing the R225X heterozygous mutation (Siu et al., 2012), and indicate that such

197 premature nonsense mutation leads to lamin A/C haploinsufficiency presumably due to nonsense-

198 mediated decay of both the lamin A and lamin C transcripts. Collectively, we established a robust *in vitro*

199 model to study cardiac laminopathy due to lamin A/C haploinsufficiency in developing cardiomyocytes.

200

201 **Lamin A/C haploinsufficiency alters hiPSC-CM automaticity and prolongs membrane**

202 **depolarization**

203 Before exploring the effect of lamin A/C haploinsufficiency on chromatin dynamics, we wished to confirm

204 a phenotypic effect on cardiac physiology in developing hiPSC-CMs. Indeed, cardiac laminopathy is a

205 disease that manifests in the third to fourth decade of life, and previous efforts to model the disease in

206 immature cardiomyocytes have been focused on studying nuclear dysmorphology, cellular senescence,

207 and susceptibility to apoptosis (Siu et al., 2012; Lee et al., 2017). Since electrical abnormalities are the

208 primary and most characteristic manifestations of cardiac laminopathy (Van Rijsingen et al., 2012;

209 Hasselberg et al., 2018; Kumar et al., 2016), we began by assessing the electrophysiological properties

210 of mutant hiPSC-CMs. For this, we first used multi-electrode arrays (MEAs) to measure the extracellular

211 electric field potential elicited by spontaneously contracting monolayers of hiPSC-CMs at day 30 of

212 differentiation. Mutant cells showed a number of alterations compared to both corrected controls. Most

213 notably, the beat rate proved highly erratic and prone to prolonged pauses (Fig. 2A). Moreover, even

214 when the analysis was focused on the periods showing the highest consistency, the beat rate was still

215 more irregular and reduced (Fig. 2B). The amplitude of field potential changes was elevated more than

216   2-fold compared to controls, which is indicative of stronger depolarizing ion currents (Fig. 2B). Along the
217   same lines, the field potential duration (FPD), which indicates the interval between depolarization and
218   repolarization, was prolonged by ~60% (Fig. 2B). This finding held true even when the FPD was corrected
219   for the beat period (FPDc; Fig. 2B), an established way to robustly compare the FPD across multiple
220   conditions (Rast et al., 2016; Asakura et al., 2015). Of note, despite all of these alterations, the conduction
221   velocity across the monolayer was not affected (Fig. 2B), indicating that intercellullar electrical coupling
222   was preserved in mutant cells.

223

224   To further characterize the electrophysiological properties of mutant hiPSC-CMs, we performed whole-
225   cell patch clamp recordings of voltage changes occurring during action potentials firing in individual
226   cardiomyocytes. To promote a mature phenotype and enhance cell viability during the invasive patch
227   procedure, we cultured hiPSC-CMs onto biomimetic anisotropic nanopatterns (Carson et al., 2016;
228   Macadangdang et al., 2015). While a number of parameters were unaffected in mutant cells (such as
229   maximum diastolic potential, action potential amplitude, mean diastolic potential, and repolarization
230   amplitude; Fig. 2D and data not shown), the action potential duration and exponential time constant for
231   the action potential decay were increased (Fig. 2C-D). This observation provided a cell-autonomous
232   explanation for the increased FPDc in cell monolayers, and indicated that this phenotype is maintained
233   in maturing hiPSC-CMs.

234

235   Finally, we measured the effects of excitation abnormalities in mutant cells on their intracellular calcium
236   dynamics using the fluorescent calcium reporter Fluo-4. Electrically-paced mutant cell monolayers
237   showed stronger and longer calcium peaks (Fig. 2E-F, Video S3, and Video S4), in agreement with MEA
238   and patch clamp data. Overall, these findings indicate that lamin A/C haploinsufficiency in developing
239   cardiomyocytes leads to altered automaticity and prolonged membrane depolarization leading to more
240   robust calcium transients.

241

242   **Systolic hyperfunction and diastolic dysfunction in lamin A/C haploinsufficient hiPSC-CMs**
243   Since changes in intracellular calcium concentrations are the primary determinant of hiPSC-CM
244   contractility, we examined the effect of lamin A/C haploinsufficiency on this process. First, we performed
245   correlation-based contraction quantification (CCQ) analyses to measure the cellular displacement
246   associated with cardiac contraction in electrically-paced hiPSC-CM monolayers (Macadangdang et al.,
247   2015). Mutant cells showed ~50% stronger contractions and a delayed relaxation time (Fig. 3A-B, Video
248   S5, and Video S6), consistent with their stronger and prolonged calcium fluxes.

249

8

250   To validate these findings in a more physiologically-relevant model, we performed biomechanical

251   assessments of contractility in electrically-paced three-dimensional engineered heart tissues (3D-EHTs),

252   an established model to promote cardiac maturation by providing topological, mechanical, and

253   multicellular cues (Leonard et al., 2018; Ruan et al., 2016). In agreement with observations in 2D

254   monolayers, mutant 3D-EHTs showed ~2-fold stronger and prolonged contractions with a markedly

255   impaired relaxation kinetic (Fig. 3C-D, Video S7, and Video S8). Collectively, we concluded that lamin

256   A/C haploinsufficiency leads to systolic hyperfunction and diastolic dysfunction in both early and maturing

257   cardiomyocytes.

258

259   **Lamin A/C haploinsufficiency causes dysregulation of specific ion channel genes and broad gene**

260   **expression changes**

261   To explore the molecular mechanisms that might explain the electrophysiological and contractile

262   phenotypes observed in lamin A/C haploinsufficient hiPSC-CMs, we first monitored the expression of the

263   genes encoding key ion-handling proteins involved in the generation of action potentials and in excitation-

264   contraction coupling (Amin et al., 2010; Eisner et al., 2017). RT-qPCR analyses excluded a dysregulation

265   of a large number of such genes, including the voltage-gated sodium channel *SCN5A*, the sodium-

266   calcium exchanger *NCX*, and the sarcoplasmic calcium ATPase *ATP2A2* (also known as SERCA2a; Fig.

267   S2D). On the other hand, mutant cells showed a significant upregulation of *CACNA1C*, and

268   downregulation of *KCNQ1* (Fig. 4A). *CACNA1C* encodes for the pore-forming subunit of L-type calcium

269   channels which mediate $I_{Ca,L}$, the main source of inward depolarizing current during phase 2 (plateau) of

270   the action potential (Bodi et al., 2005). On the other hand, I_{KS}, the outward potassium current resulting

271   from the potassium channel encoded by *KCNQ1*, antagonizes $I_{Ca,L}$ in phase 2 by initiating membrane

272   repolarization (Peroz et al., 2008). Thus, the combined effects of *CACNA1C* upregulation and *KCNQ1*

273   downregulation could explain the prolonged membrane depolarization observed in mutant cells.

274

275   We then expanded these gene expression analyses genome-wide by performing RNA sequencing of

276   hiPSC-CM monolayers at day 14 of differentiation on biological triplicates (RNA-seq; Table S1). While

277   cells from the two corrected control lines clustered closely and showed remarkably similar gene

278   expression profiles (29 upregulated and 71 downregulated genes between Corr.1 and Corr.2; fold-

279   change > 2 and q-value < 0.05; Fig. 4B and Table S1), mutant cells clustered separately due to

280   substantial gene up- and downregulation (Fig. 4B-C and Table S1). To increase the robustness of our

281   subsequent analyses, we only considered genes as dysregulated if they had significant expression

282   changes in mutant hiPSC-CMs *versus* both corrected controls (185 upregulated and 140 downregulated;

283   Fig. 4C and Table S1). Ontology and pathway enrichment analyses on these gene lists revealed that

9

284 upregulation in mutant cells was significantly associated with: (1) focal adhesion, MAPK, and TGFß
285 pathways; (2) transcriptional activation, positive regulation of cardiac differentiation, and inhibition of
286 apoptosis; (3) non-cardiac lineage expression (such as fibroblast and smooth muscle; Fig. 4D and Table
287 S2). Notable examples of genes within these categories include: (1) *PDGFA*, *EGF*, and *GDF7*; (2) *TBX3*,
288 *TBX20*, and *HAND1*, (3) *CTGF/CCN2*, *MYH9*, and *ACTA2*. In contrast, downregulated genes were
289 enriched in cardiac transcripts and factors involved in cardiomyopathy and PI3K pathways, such as
290 *TNNT3*, *TNNI3*, *SGCA*, *NGFR*, and *PDGFD* (Fig. 4D and Table S2). We also compared these RNA-seq
291 data with those we recently obtained from human embryonic stem cells (hESCs) profiled at different time
292 points of cardiac differentiation (Fields et al., 2017). Linear dimensionality reduction by principal
293 component analysis showed that both mutant and corrected hiPSC-CMs clustered closely to hESC-CMs
294 (Fig. 4E). This indicated that despite dysregulation of >300 genes, mutant hiPSC-CMs were not globally
295 developmentally delayed from a transcriptional standpoint. These data suggest that lamin A/C
296 haploinsufficiency in developing hiPSC-CMs leads to dysregulation of multiple signaling pathways, in
297 agreement with earlier findings from mouse models (Arimura et al., 2005; Muchir et al., 2007; Ramos et
298 al., 2012; Choi et al., 2012). Further, it prevents efficient silencing of some cardiac developmental
299 regulators and alternative lineage genes, while specific cardiac genes are not fully activated.

300

301 **Lamin A/C haploinsufficiency strengthens the separation between chromosome territories and**
302 **between chromatin compartments**
303 Having established that lamin A/C haploinsufficiency results in marked changes in both gene expression
304 and cellular physiology in developing hiPSC-CMs, we tested whether some of these phenotypes could
305 be explained by changes in chromatin topology. In order to explore this aspect at a genome-wide level,
306 we took advantage of *in situ* DNase Hi-C to capture all pairwise interactions between any two genomic
307 regions (Ramani et al., 2016). We analyzed two independent batches of hiPSC-CMs at day 14 of
308 differentiation from the mutant and two corrected lines, and we confirmed that the resulting Hi-C data
309 were of high quality and reproducible across biological replicates, with samples clustering separately
310 based on their genotype (Fig. 5A and Table S3). We then began exploring the global properties of
311 chromatin topology and noticed that mutant cells showed an increased ratio of genomic interactions with
312 the same chromosome (in *cis*) over those involving different chromosomes (in *trans*; Fig. 5B). Moreover,
313 *trans* interactions were distributed differently: while all hiPSC-CMs showed the expected pattern of
314 preferential self-association between small, gene-rich chromosomes (especially chromosomes 16, 17,
315 19, 20, and 22) and between large, gene-poor chromosomes (such as chromosomes 1 to 8; Fig. S3A;
316 Lieberman-Aiden et al., 2009), this property was even more striking in mutant cells (Fig. 5C). On the
317 contrary, interactions between small and large chromosomes were less frequent (Fig. 5C). Thus, lamin

318   A/C haploinsufficiency reinforces the separation between chromosome territories and their segregation

319   based on size and gene density.

320

321   We then analyzed the separation of chromatin domains into the active (A) or inactive (B) compartment.

322   For this, we computed the first principal component (PC1) from the contact matrix using bins of 500 Kb

323   (Table S4), a well-established method to determine chromatin compartments based on their preferential

324   association (Imakaev et al., 2012; Lieberman-Aiden et al., 2009). In agreement with our previous

325   observations in hESC-CMs (Fields et al., 2017), *trans* interactions between chromatin domains favored

326   A-A compartments, and this was not affected by lamin A/C haploinsufficiency (Fig. S3B). In *cis*, mutant

327   cells showed stronger interactions between A-A compartments (Fig. 5D and Fig. S3B), particularly due

328   to increased short-range contacts within 0.5-1 Mb (Fig. 5E). In contrast, interactions between heterotypic

329   regions (A-B) were reduced in mutant cells (Fig. 5D and Fig. S3B), particularly for long-range contacts

330   >10 Mb (Fig. 5E). Collectively, lamin A/C haploinsufficiency reinforces the separation between the active

331   and inactive chromatin compartments.

332

333   **Incomplete transitions from the active to inactive chromatin compartment in lamin A/C**

334   **haploinsufficient hiPSC-CMs**

335   To assess the effect of lamin A/C haploinsufficiency on chromatin compartmentalization, we identified

336   genomic bins with significantly different A/B compartment scores and switching from active to inactive or

337   *vice versa* between at least two conditions (Table S4). We noticed that the vast majority of compartment

338   transitions were observed for mutant hiPSC-CMs *versus* each corrected control (Fig. 6A), and that B to

339   A inversions were more common than A to B ones (42 and 27, respectively; Table S4). We observed

340   that, 63% of A to B transitions in mutant cells involved the X chromosome, while B to A changes showed

341   a notable concentration on chromosome 19 but were otherwise evenly spread across 13 additional

342   chromosomes (Fig. 6B, Fig. S4A, and Table S4). Overall, compartment changes involved approximately

343   1.2% of the genome, indicating that chromatin compartment dysregulation in mutant cells is not

344   widespread but is actually highly restricted.

345

346   To gain insight into the relationship between dysregulated regions and normal chromatin compartment

347   dynamics during cardiomyocyte differentiation, we integrated Hi-C data from mutant and corrected

348   hiPSC-CMs with those we previously generated at different time points throughout hESC-CM

349   differentiation (Fields et al., 2017). Linear dimensionality reduction of A/B compartment scores for all

350   samples confirmed that mutant hiPSC-CMs cluster separately from both corrected controls (Fig. 6C).

351   Moreover, this analysis revealed that based on the first principal component (which explained 39% of the

11

352   variance and ordered hESC samples based on their developmental progression), mutant cells were
353   mildly developmentally delayed from a chromatin compartmentalization standpoint (Fig. 6C). Accordingly,
354   we observed a strong and significant enrichment for domains that normally transition from A to B during
355   cardiac differentiation but remain in A in mutant cells (Fig. 6D). Notable examples of such behavior
356   involved two 0.5 and 2.5 Mb-long portions of chromosome 19 (corresponding to 19p13.13 and 19q13.33,
357   respectively), and a 1 Mb region on chromosome 5 (5q31.3; Fig. 6B and 6E). We also observed a weaker
358   enrichment for the opposite dynamic (impaired B to A transitions; Fig. 6D), but we note that this analysis
359   was limited to autosomes since compartment transitions of the X chromosome could not be assessed in
360   female hESC-CMs due to the confounding factor of X inactivation (Fields et al., 2017). In sum, lamin A/C
361   haploinsufficiency in developing hiPSC-CMs results in highly selective dysregulation of chromatin
362   compartmentalization, particularly for a handful of genomic hotspots that fail to transition from the active
363   to inactive compartment. We will refer to these as lamin A/C-sensitive B domains.

364

365   **Dysregulation of lamin A/C-sensitive B domains leads to ectopic expression of non-cardiac genes**
366   We then assessed the functional consequences of compartment dysregulation due to lamin A/C
367   haploinsufficiency. Strikingly, we observed almost no overlap between genes within lamin A/C-sensitive
368   domains and genes significantly and strongly up- or downregulated in mutant cells (Fig. S4B).
369   Accordingly, there were no significant changes in the average expression of genes found in lamin A/C-
370   sensitive domains in mutant *versus* corrected controls (Fig. 7A). Nevertheless, we noticed a small number
371   of genes located in lamin A/C-sensitive B domains that were expressed at very low levels in corrected
372   hiPSC-CMs and upregulated in mutant cells (29 genes with an average fold-change > 2; Fig. 7A and Fig.
373   S4C). These genes were significantly enriched for three chromosome locations (Fig. 7B), two of which
374   corresponded to the lamin A/C-sensitive hotspots 5q31.3 and 19q13.33 (Fig. 6E), and were associated
375   with neuronal development (Fig. 7B, and Table S5).

376

377   Of note, most genes in the group just described had not been determined as differentially expressed
378   based on RNA-seq analysis using Cufflinks since lowly-expressed genes are subject to strong negative
379   penalization when calculating the q score due to the challenges in robustly assessing their expression
380   (Trapnell et al., 2012, 2010). This explains their absence in the lists used for the overlap shown in
381   Supplemental Figure 4B. To increase our confidence with these results we validated the expression of
382   several genes within this class by RT-qPCR. Moreover, to exclude that such gene expression differences
383   were simply explained by a differentiation delay in mutant hiPSC-CMs, we analyzed hiPSC-CMs matured
384   either by longer 2D culture or by the generation of 3D-EHTs. Remarkably, nearly all genes tested showed
385   consistent significant upregulation in mutant samples (Fig. 7C-D and Fig. S4D-E). These findings

386   confirmed that impaired transition to the B compartment of selected lamin A/C-sensitive domains leads

387   to upregulation of multiple non-cardiac genes that would otherwise be silenced during cardiomyocyte

388   differentiation.

389

390   **Ectopic P/Q-type and potentiated L-type calcium currents contribute to electrophysiological**

391   **abnormalities of lamin A/C haploinsufficient hiPSC-CMs**

392   Genes found in lamin A/C-sensitive B domains and upregulated in mutant hiPSC-CMs included multiple

393   factors with either unknown function, such as the putative uncharacterized protein C19orf81, or with

394   established roles in the nervous system but not normally expressed in the heart (Fig. 7C-D and Fig. S4D-

395   E). This group included genes from all of the three protocadherin clusters on chromosome 5 (alpha, beta,

396   and gamma, exemplified by *PCDHA10*, *PCDHB15*, and *PCHDGB4*; Chen and Maniatis, 2013), *LRRC4B*

397   (encoding for the postsynaptic cell adhesion molecule NGL-3; Maruo et al., 2017), *SYT3* (involved in

398   postsynaptic endocytosis; Awasthi et al., 2018), and *CACNA1A* (which encodes for the pore-forming

399   subunit of neuronal P/Q-type calcium channels; Rajakulendran et al., 2012).

400

401   *CACNA1A* appeared particularly interesting given the prolonged action potential duration observed in

402   mutant hiPSC-CM populations. Indeed, the depolarizing $I_{Ca,P}$ and $I_{Ca,Q}$ currents resulting from the protein

403   product of *CACNA1A* are known to be strong and long-lasting, even more so than $I_{Ca,L}$ currents typical of

404   hiPSC-CMs (Catterall et al., 2005; Nimmrich and Gross, 2012). Thus, we tested whether $I_{Ca,P}$ and $I_{Ca,Q}$

405   currents contributed to the electrophysiological abnormalities of mutant cells by inhibiting such currents

406   using two structurally unrelated highly-specific inhibitors derived from spider venoms: ω-Conotoxin MVIIC

407   and ω-Agatoxin TK (Adams et al., 1993; McDonough et al., 1996; Nimmrich and Gross, 2012). MEA

408   experiments demonstrated that both toxins led to a modest but significant decrease in the FPDc in

409   monolayers of mutant hiPSC-CMs, while they did not affect their depolarization amplitude (Fig. 8A-B).

410   On the other hand, neither toxin had a significant effect on the FPDc in corrected controls (Fig. 8A-B),

411   confirming that $I_{Ca,P}$ and $I_{Ca,Q}$ currents do not play a role in cardiac depolarization in physiological

412   conditions, and establishing that the toxins had no overt non-specific effects on hiPSC-CM

413   electrophysiology at the doses tested. These experiments indicated that ectopic expression of *CACNA1A*

414   in mutant cells and the resulting P/Q-type calcium currents contribute to the prolonged depolarization

415   observed in lamin A/C haploinsufficient hiPSC-CMs.

416

417   As mentioned above, we also observed *CACNA1C* upregulation and *KCNQ1* downregulation in mutant

418   hiPSC-CMs at day 14 of differentiation (Fig. 4A). RT-qPCR analyses in hiPSC-CMs matured for a longer

419   period in 2D monolayers or in 3D-EHTs indicated that *KCNQ1* downregulation was specific to early

13

420   hiPSC-CMs (Fig. 8C-D). On the other hand, upregulation of *CACNA1C* was maintained in more mature

421   hiPSC-CMs (Fig. 8C-D). Of note, *CACNA1C* is a gene always found in the A chromatin compartment

422   throughout hiPSC-CM differentiation (Fields et al., 2017), and such localization was unaltered in mutant

423   hiPSC-CMs (Table S4). Given the established role of $I_{Ca,L}$ in the development and maintenance of the

424   cardiac action potential (Catterall et al., 2005), we tested if its inhibition with the L-type calcium blocker

425   verapamil could revert the electrophysiological abnormalities of mutant hiPSC-CMs. Remarkably, low

426   concentrations of verapamil markedly reduced both the FPDc and the spike amplitude of mutant hiPSC-

427   CM monolayers, while they had little or no effect on corrected controls (Fig. 8E). Overall, we conclude

428   that the combination of ectopic P/Q-type calcium currents due to aberrant chromatin compartment

429   dynamics, and of enhanced L-type calcium currents *via* other epigenetic mechanisms lead to the

430   electrophysiological abnormalities of lamin A/C haploinsufficient hiPSC-CMs (Fig. 8F).

431

432   **Discussion**

433

434   **Disease modeling of cardiac laminopathy in developing cardiomyocytes**

435   Previous efforts to study cardiac laminopathy using patient-derived hiPSCs have relied on hiPSCs from

436   unrelated healthy subjects as controls (Siu et al., 2012; Lee et al., 2017), a strategy which has known

437   limitations (Sala et al., 2017). By developing a method to generate isogenic control hiPSCs through

438   entirely scarless gene correction we provide a more rigorous *in vitro* model of cardiac laminopathy due

439   to lamin A/C haploinsufficiency, which we apply to broaden our understanding of the disease with respect

440   to cardiac electrophysiology and contractility.

441

442   Because the earliest manifestation of cardiac laminopathy is severe electrical abnormalities in the

443   myocardium (Van Rijsingen et al., 2012; Hasselberg et al., 2018; Kumar et al., 2016), our observations

444   of aberrant electrophysiological properties in mutant hiPSC-CMs may be noteworthy. While alterations in

445   cardiac rhythm could have been anticipated given the clinical manifestations of this disease, we were

446   surprised to note increased FPDc and action potential duration. The FPD is the *in vitro* analogue of the

447   QT interval measured by electrocardiogram (which indicates the interval between ventricular

448   depolarization and repolarization). Genetic or acquired prolongation of QT interval is a strong risk factor

449   for development of severe arrhythmias (Vandael et al., 2017), and QT interval prolongation has been

450   reported in patients with *LMNA* mutations causing cardiac laminopathy (Pan et al., 2009), Emery-Dreifuss

451   muscular dystrophy (Russo et al., 2012), and Hutchinson-Gilford progeria syndrome (Merideth et al.,

452   2008). Although prolonged QT has not been widely described as a hallmark of cardiac laminopathy, we

453   speculate that this could be an underappreciated early clinical phenotype. Prolonged QTc and

454 subsequent increase in calcium influx might predispose patients to cardiac arrhythmias and/or could be
455 an early marker of a broader conduction system disease.

456

457 A striking phenotype of the laminopathic cardiomyocytes was their enhanced contractility in monolayers
458 and in engineered heart tissues. Increased contractility can be explained by the prolonged action
459 potentials and stronger calcium fluxes that these myocytes exhibit. At a first glance, greater contractility
460 might appear to conflict with the clinical phenotype of some laminopathy patients who develop systolic
461 heart failure. However, in contrast to the early-onset and highly penetrant malignant conduction disease,
462 left ventricular dilatation and systolic failure is experienced by just a fraction of cardiac laminopathy
463 patients and only after years after the initial diagnosis (Van Berlo et al., 2005; Kumar et al., 2016; Tobita
464 et al., 2018). Moreover, heart failure is a complex disease that involves multiple cell types as well as the
465 extracellular matrix (Metra and Teerlink, 2017). Thus, we propose that the systolic hyperfunction and
466 diastolic dysfunction of lamin A/C haploinsufficient hiPSC-CMs might reflect an early and cell-
467 autonomous phenotype of cardiac laminopathy, which over the years can evolve into an organ-level
468 disease characterized by decreased systolic function. A possible mechanism for this could be the chronic
469 calcium overload in laminopathic cardiomyocytes, as this is a well-established stimulus that can lead to
470 dilated cardiomyopathy due to activation of signaling pathways such as calcineurin/NFAT (Molkentin et
471 al., 1998; Nakamura et al., 2008; Zhang et al., 2016). Additionally, it was previously shown that
472 laminopathic cardiomyocytes are highly sensitive to apoptosis (Ho et al., 2011; Lee et al., 2017), which
473 could over the years contribute to the development of severe cardiac fibrosis that is typical in cardiac
474 laminopathy patients (van Tintelen et al., 2007b; Fontana et al., 2013; Tobita et al., 2018). A corollary of
475 these intriguing hypotheses is that medical interventions during the early phases of the disease, such as
476 the use of calcium antagonists and/or anti-apoptotic agents (Lee et al., 2014; Nie et al., 2018), may be
477 able to prevent the development of heart failure in cardiac laminopathy patients.

478

479 **Chromatin architecture changes in lamin A/C haploinsufficient cardiomyocytes**
480 Our study's primary goal was to study the pathogenesis of cardiac laminopathy. Nevertheless, by
481 integrating Hi-C results from lamin A/C haploinsufficient and control hiPSC-CMs with our previous Hi-C
482 dataset at different stages of human cardiogenesis (Fields et al., 2017), we were also able to shed light
483 on the physiological roles of lamin A/C during cardiac specification. We observed that lamin A/C
484 haploinsufficiency reduces inter-chromosomal interactions, reinforces the separation between small and
485 large chromosomes, increases the long-range segregation of A and B chromatin compartments, and
486 strengthens short-range homotypic interactions within the A compartment. Intriguingly, most of these
487 effects antagonize the chromatin organization dynamics that normally occur during human cardiogenesis

15

488   (Fields et al., 2017). These data demonstrate that lamin A/C is an important mediator of physiological

489   changes in nuclear architecture during differentiation, in agreement with its gradual upregulation as cells

490   exit the pluripotent state and commit to the cardiac lineage.

491

492   The major hypothesis going into this study was that lamin A/C haploinsufficiency would induce

493   widespread gene dysregulation due to inappropriate A/B compartmentalization, the so-called "chromatin

494   hypothesis" for the pathogenesis of cardiac laminopathy (Worman and Courvalin, 2004; Cattin et al.,

495   2013). This hypothesis was not robustly supported. RNA-seq analysis showed that only ~325 genes were

496   up- or down-regulated in laminopathic cardiomyocytes. Analysis of A/B compartment changes revealed

497   that only ~1.2% of the genome changed compartments in *LMNA* mutants, and these aberrations were

498   concentrated in hotspots on chromosomes 5 and 19. Surprisingly, the overlap between strong

499   dysregulation in gene expression and compartment aberrations was minimal (less than 2%; Fig. S4B).

500   As discussed below, the *CACNA1A* gene is ectopically expressed and resides in an A compartment that

501   fails to silence during differentiation. Thus, while examples can be found that may contribute to disease,

502   most of the transcriptional dysregulation appears to result from factors other than errors in

503   compartmentalization. Overall, these findings do not support the "chromatin hypothesis" for the

504   pathogenesis of cardiac laminopathy. On the other hand, our results agree with previous findings from

505   mouse embryonic stem cells (mESCs), in which depletion of B-type nuclear lamins results in minimal

506   changes in A/B compartmentalization (Amendola and van Steensel, 2015; Zheng et al., 2015, 2018). Our

507   results establish that while A-type lamins seem to participate in chromatin organization in developing

508   cardiomyocytes, lamin A/C haploinsufficiency leads to only modest alterations in A/B

509   compartmentalization even in mechanically active cells.

510

511   Interestingly, we identify *CACNA1A* as a disease-associated gene linked to alterations of A/B

512   compartmentalization. *CACNA1A* is normally expressed throughout the nervous system with the highest

513   expression on Purkinje neurons in the cerebellum and in cerebellar granular cells (Nimmrich and Gross,

514   2012). Its ectopic expression and the modest contribution of the resulting P/Q-type calcium currents on

515   FPDc prolongation in lamin A/C haploinsufficient hiPSC-CMs suggests that this may represent a

516   therapeutic target to ameliorate the electrical abnormalities in the myocardium of cardiac laminopathy

517   patients. Further assessments of *CACNA1A* expression in patient-derived primary samples will be of high

518   interest. We also identified the locus containing the three protocadherin clusters as another lamin A/C-

519   sensitive B domain associated to ectopic gene expression. Protocadherin genes are well-established

520   mediators of accurate neuronal connectivity, and are not normally expressed in the heart (Hayashi and

521   Takeichi, 2015). It is an intriguing possibility that ectopic protocadherin expression may change cellular

16

522   adhesion patterns in the cardiac conduction system, which may contribute to conduction disease in
523   cardiac laminopathy. Other interesting targets of chromatin compartment dysregulation in lamin A/C
524   haploinsufficient hiPSC-CMs are GPC4, whose upregulation might explain the incomplete silencing of
525   cardiac progenitor genes (Strate et al., 2015), and CLEC11A (also known as stem cell growth factor), a
526   cytokine normally involved in bone marrow homeostasis but upregulated in cardiac disease (Wang et al.,
527   2013).

528

529   If chromatin compartment alterations do not directly explain the majority of gene expression changes
530   observed in lamin A/C haploinsufficient hiPSC-CMs, what is driving these changes? An important
531   example of ths behaviour is *CACNA1C*, which is upregulated in mutant cells while not changing
532   compartmentalization. At least two non-exclusive possibilities come to mind. First, it remains possible
533   that alterations in chromatin organization play a primary role, albeit not in the form of outright changes in
534   A/B compartmentalization. For instance, it was reported that B-type lamins can indirectly affect the
535   expression of genes within the nuclear interior by affecting the interaction between TADs as a
536   consequence of distal alterations in LAD compaction (Zheng et al., 2018). It is thus possible that A-type
537   lamins might have a similar role, which will be interesting to test in detail in future studies. A second
538   possibility for compartment-independent gene expression changes might be the result of changes in
539   intracellular signaling pathways such as MAPK and mTOR. Indeed, such pathways have well-established
540   links with the nuclear lamina (Dobrzynska et al., 2016), and are upregulated in animal models of cardiac
541   laminopathy (Muchir et al., 2007, 2012; Choi et al., 2012).

542

543   Emerging evidence suggests that nonsense/haploinsuffiency mutations in *LMNA* may have a different
544   pathogenesis than missense mutations. We have recently collaborated to study a previously described
545   heterozygous K219T missense mutation in *LMNA* (Roncarati et al., 2013). Interestingly, this mutation
546   leads to distinct electrophysiological abnormalities, namely reduced peak sodium current and diminished
547   conduction velocity, which are caused by downregulation of *SCN5A* as result of closer proximity to the
548   nuclear lamina and increased H3K27me3 (Salvarani, Crasto et al., manuscript in preparation). In the
549   current study we have not observed a similar reduction of *SCN5A* expression in lamin A/C
550   haploinsufficient hiPSC-CMs (Fig. S2D). Furthermore, our Hi-C data indicate that the *SCN5A* gene is
551   found in a chromatin domain which is always part of the A compartment both throughout normal cardiac
552   differentiation (Fields et al., 2017) and in lamin A/C haploinsufficient hiPSC-CMs (Table S4). These
553   observations prompt the intriguing hypothesis that haploinsufficient and missense mutations in *LMNA*
554   might lead to cardiac laminopathy *via* distinct molecular mechanisms.

555

17

556   In conclusion, our work establishes that while lamin A/C haploinsufficient hiPSC-CMs show marked

557   alterations in electrophysiology, contractility, and chromosomal topology, phenotypic changes cannot, for

558   the most part, be directly explained by alterations in chromatin compartmentalization. With this in mind,

559   it is important to mention that this study does not come without limitations. We acknowledge that modeling

560   diseases of the adult heart in immature hiPSC-CMs suffers from inherent drawbacks. It is possible that

561   functional chromatin dysregulation could be more important in adult myocytes subjected to high levels of

562   mechanical stress *in vivo*. Addressing this aspect will require substantial advances in our ability to mature

563   hiPSC-CMs and/or improvements of genome-wide chromatin conformation capture technologies in order

564   to reliably measure chromatin architecture from small numbers of myocytes isolated from precious

565   primary samples. Furthermore, future studies will be required to test whether other types of mutations

566   (such as missense changes like the aforementioned K219T mutation) result in more substantial genome-

567   wide alterations in chromatin topology than what was observed following lamin A/C haploinsufficiency.

568   All considered, our work provides a stepping stone towards understanding the relevance of the

569   "chromatin hypothesis" in the pathogenesis of cardiac laminopathy, while it also sheds light on the

570   physiological roles of A-type lamins in the chromatin dynamics that accompany human cardiogenesis.

571

572   **Materials and methods**

573

574   **hiPSC culture and differentiation**

575   Human induced pluripotent stem cells (hiPSCs) were cultured and differentiated into cardiomyocytes

576   (hiPSC-CMs) with minor modifications of previously described methods (Burridge et al., 2014; Fields et

577   al., 2017). hiPSCs were cultured on plates pre-coated with 0.5 μg/cm^2 recombinant human Laminin-521

578   matrix (rhLaminin521; Biolamina) with daily changes of antibiotic-free Essential 8 (E8) media

579   (ThermoFisher). Cells were passaged as small clumps with Versene (ThermoFisher), and 10 μM Y-27632

580   (Tocris) was added for the first 16 hr.

581

582   For hiPSC-CM generation, cells were passaged as single cells with Versene, and seeded at a density of

583   2.5 x 10^5 per well of a 12-well plate pre-coated with 2 μg/cm^2 rhLaminin521 (denoted day -2). After 24 hr

584   media was changed to E8 with 1 μM CHIR-99021 (Cayman), denoted day -1. On day 0 media was

585   changed to RBA media (RPMI 1640 with glutamine [ThermoFisher] supplemented with 500 μg/ml BSA

586   and 213 μg/ml ascorbic acid [both from Sigma-Aldrich]) supplemented with 4 μM CHIR-99021. At day 2,

587   media was changed to RBA with 2 μM WNT-C59 (Selleckchem). On day 4, media was changed to RBA.

588   On day 6, media was changed to RPMI-B27 media (RPMI with 1x B-27 supplement, both from Thermo

589 Fisher), with further media changes every other day. Beating was first observed between day 7 and day

590 9, and cells were cultured until day 14 before collection (unless otherwise indicated). hiPSC-CMs to be

591 used for functional assays of cardiac electrophysiology or contractility were preconditioned with a 30 min

592 heat-shock at 42º on day 13, and cryopreserved at day 14 following single-cell dissociation using 0.25%

593 w/vol Trypsin (ThermoFisher) in Versene.

594

595 Frozen hiPSC-CM stocks were thawed and seeded at a density of 2 x 10^5 cells/cm^2 onto rhLamin521 pre-

596 coated dishes (2 μg/ml) in RPMI-B27, which was supplemented with 10 μM Y-27632 and 5% FBS

597 (ThermoFisher) for the first 16 hr. hiPSC-CMs were then cultured in RPMI-B27 with media changes every

598 other day. After one week (day 21 of differentiation), hiPSC-CMs were dissociated to single cell using

599 0.05% Trypsin-EDTA (ThermoFisher), and seeded at the desired density the downstream assays.

600

601 **Gene editing**

602 hiPSCs with a heterozygous c.672C>T mutation in the *LMNA* gene (resulting in p.Arg225*, or R225X)

603 were generated through lentiviral reprogramming of dermal fibroblasts from a 56 year-old male patient

604 with severe cardiac laminopathy (Siu et al., 2012). Cells were obtained at passage 29, adapted to culture

605 in E8/rhLaminin521, and banked at passage 34. These hiPSC stocks were confirmed to be Mycoplasma

606 negative (MycoAlert Detection Kit, Lonza), and proved euploid by conventional G-banding karyotyping

607 (Diagnostic Cytogenetics Inc, Seattle). Cell identity was tested by Sanger sequencing of a genomic PCR

608 product for exon 4 of *LMNA* (PCR primers: 5'- GGCTGGGTGATGACAGACTT-3' and 5'-

609 TACTGCTCCACCTGGTCCTC-3'; sequencing primer 5'- GCCCTAGTGGACAGGGAGTT-3'), which

610 confirmed the expected c.672C>T heterozygous mutation.

611

612 The mutation was corrected into the wild-type allele by adapting a previously described two-step method

613 for scarless genome editing relying on CRISPR/Cas9-facilitated homologous recombination of a targeting

614 vector containing the wild-type allele in one homology arm, and an excisable piggyBac drug resistance

615 cassette (Fig. S1A; Yusa, 2013; Yusa et al., 2011). Since the c.672C>T mutation lies close to the 3' splice

616 acceptor site of exon 4 (Fig. S1B), we reasoned that any intergenic mutation could have poorly

617 predictable effects on *LMNA* splicing. To avoid any kind of genomic scar, we identified a suitable

618 endogenous "TTAA" site in the third intron of *LMNA* and located 151 bp upstream to the c.672C>T

619 mutation in exon 4 (Fig. S1B). Further, we designed single guide RNAs (sgRNAs) spanning such TTAA

620 site, so that only the endogenous allele could be cut by CRISPR/Cas9. This strategy allowed us to avoid

621 inserting any additional mutation onto one of homology arms in the targeting vector (such as those

622 classically used to disrupt the PAM site). Two sgRNAs were designed using mit.crispr.edu, and had a

623 score higher than 75%, indicating a very high *in-silico* predicted specificity (sgRNA 1: 5'-
624 CTACCAGCCCCACTTTAACC-'3 and sgRNA2 5'-TCAGCTCCCAGGTTAAAGTG-3', sequences without
625 PAM site). To further decrease the risk of CRISPR/Cas9 off-target activity, we adopted the enhanced
626 specificity *Streptococcus Pyogenes* Cas9 (eSpCas9) developed by Dr. Feng Zhang and colleagues
627 (Slaymaker et al., 2015). The sgRNA was cloned into the eSpCas9(1.1) plasmid (Addgene #71784) using
628 a standard method based on restriction digestion with BbsI followed by ligation of a double-stranded oligo
629 (Ran et al., 2013). The resulting plasmids were named eSpCas9(1.1)_LMNA_sgRNA1 and
630 eSpCas9(1.1)_LMNA_sgRNA2. The sequences were confirmed by Sanger sequencing, and the sgRNAs
631 were validated to have a high on-target activity as measured by T7E1 assay in HEK293 cells (which was
632 comparable to that observed using wild-type SpCas9).

633

634 The *LMNA* targeting vector was constructed starting from the MV-PGK-Puro-TK_SGK-005 plasmid
635 (Transposagen), which contains a piggyBac transposon encoding for a PGK-EM7 promoter-driven dual
636 positive/negative selection cassette (puromycin N-acetlytransferase, ensuring resistance to puromycin,
637 and truncated *Herpes simplex* virus thymidine kinase, conferring sensitivity to ganciclovir or its analog
638 fialuridine). First, the piggyBac cassette was excised using NsiI and BsiWI and isolated. Then, a
639 backbone with ends suitable for the subsequent overlap-based assembly was obtained from this same
640 plasmid after removal of the piggyBac cassette using NotI and AscI. Finally, these two fragments were
641 re-assembled together with two PCR products representing the 5' and 3' homology arms to the *LMNA*
642 gene. The two homology arms were approximately 1 Kb long, and were amplified from genomic DNA of
643 RUES2 human embryonic stem cells (hESCs) using primers: 5'- GGTCCCGGCATCCGATACCCAATG-
644 GCGCGCCCGTACTTCAGGCTTCAGCAGT-3' and 5'- AAAGAGAGAGCAATATTTCAAGAATGCATG-
645 CGTCAATTTTACGCAGACTATCTTTCTAGGGTTAACCTGGGAGCTGAGTGC-3' (for the 5' homology
646 arm); 5'- AATTTTACGCATGATTATCTTTAACGTACGTCACAATATGATTATCTTTCTAGGGTTAAAGT-
647 GGGGCTGGTAGTG-3' and 5'-CGAATGCGTCGAGATATTGGGTCGCGGCCGCCCTGTCACAAATAG-
648 CACAGCC-3' (for the 3' homology arm), and Q5 High-Fidelity DNA Polymerase (New England Biolabs)
649 according to the manufacturer's instructions. The four-way assembly reaction was performed using
650 NEBuilder HiFi DNA Assembly Kit (New England Biolabs) according to the manufacturer's instructions,
651 and the resulting targeting plasmid was named pbLMNA_R225R. Sanger sequencing confirmed that the
652 3' homology arm contained the wild-type R225R allele, while the remaining genomic sequence of both
653 homology arms was identical to that of the R225X hiPSC line as no SNPs were identified. The cloning
654 strategy was designed so that during PCR the "TTAA" site was inserted both at the end of the 5' homology
655 arm and at the start of the 3' homology arm, ensuring that the piggyBac cassette contained within could

656   be excised using transposase while leaving behind a single "TTAA" matching the original genomic
657   sequence (Fig. S1A).

658

659   For the first gene targeting step, 7.5 x 10^4 hiPSCs were seeded in each well of 6-well plate and
660   immediately transfected using GeneJuice (Millipore) according to the manufacturer's instructions. Briefly,
661   for each well 3 μl of GeneJuice was mixed with 100 μl of Opti-MEM (ThermoFisher Scientific) and
662   incubated for 5 min at room temperature. 1 μg of DNA was added to the transfection solution (equally
663   divided   between   pbLMNA_R225R   and   either   eSpCas9(1.1)_LMNA_sgRNA1   or
664   eSpCas9(1.1)_LMNA_sgRNA2), which was further incubated for 15 min at room temperature and finally
665   added to the cell suspension. After 16 hr from transfection, cells were washed with DPBS and cultured
666   for another 3 days. Gene targeted cells were selected by adding 1 μg/ml puromycin to the media for 4
667   days, after which the dose was reduced to 0.5 μg/ml. 10 μM Y-27362 was added for the first 48 hr of
668   selection. Puromycin was then maintained at all times until the second gene targeting step to prevent
669   silencing of the piggyBac transgene. After 7 days from the transfection, 10-15 individual and well-
670   separated colonies could be identified in each well of 6-well plate, indicating that they likely arose from
671   clonal expansion of a single gene-edited hiPSC. Colonies were manually picked following gentle
672   treatment with Versene to facilitate their detachment from the matrix, and individually expanded as
673   individual lines. Clones were screened by genomic PCR using LongAmp Taq Polymerase (New England
674   Biolabs) according to manufacturer's instructions, except that all reactions were performed using an
675   annealing temperature of 63 °C and an extension time of 2 min. The primer sequences are reported in
676   Supplemental Table 6, and the genotyping strategies are illustrated in Supplemental Figure 1. Briefly,
677   junctional PCRs for both the 5' and 3' integration site (5'- and 3'-INT) were used to confirm site-specific
678   integration, while locus PCRs were used to monitor the presence of residual wild-type alleles. This
679   allowed to discriminate homozygous clones from heterozygous ones or mixed cell populations. Finally,
680   PCRs of the targeting vector backbone (5'- and 3'-BB) were performed to exclude random integration of
681   the plasmid elsewhere in the genome. Homozygous clones with only on-target integration events were
682   selected (3 out of 18 and 2 out of 24 for sgRNA 1 and sgRNA 2, respectively). These positive clones
683   were further characterized by Sanger sequencing of the 5'- and 3'-INT PCR products to confirm the
684   presence of the wild-type R225R allele in homozygosity (found in all of the 5 lines) and exclude other
685   unwanted mutations elsewhere in the locus (absent in all 5 lines). Two clones (one for each sgRNA) were
686   karyotyped by standard G-banding, which confirmed their euploidy, and were therefore selected for the
687   second gene targeting step. These clones were named pb R225R g1 and pb R225R g2 (Fig. S1C).

688

689   To remove the piggyBac and restore the *LMNA* locus to its original form, pb R225R g1 and pb R225R g2

690   hiPSCs were transfected as described above but using 1 µg of excision-only piggyBac transposase

691   expression vector (PBx; Transposagen). Puromycin was removed from the media the day before

692   transfection, and subsequently omitted. After 3 days from the transfection, the populations were

693   passaged as single cells, and 1 x 10^4 cells were seeded per 10 cm plate in the presence of 10 µM Y-

694   27362. On the next day, negative selection of cells still possessing the piggyBac cassette was initiated

695   by adding 200 nM fialuridine. 10 µM Y-27362 was added for the subsequent 48 hr. Selection was

696   complete after 5 days, at which point 10-50 individual and well-separated colonies could be identified in

697   each 10 cm dish. Individual colonies were isolated, clonally expanded, and screened by genomic PCR

698   as described above to identify those with homozygous reconstitution of the wild-type allele (5 out of 30

699   and 6 out of 39 for sgRNA 1 and sgRNA2, respectively). These were further characterized by sequencing

700   to ensure that the sequence surrounding the "TTAA" site was faithfully reconstituted upon piggyBac

701   excision (confirmed in a subset of 4 lines, 2 for each sgRNA; Fig. S1C-D). Two clones (one for each

702   sgRNA), were karyotyped by standard G-banding, which confirmed their euploidy, and therefore selected

703   for subsequent functional experiments. These clones were named R225R g1-15 and R225R g1-38, and

704   are referred to in the text and figures as Corrected 1 and Corrected 2 (or Corr.1 and Corr.2).

705

706   Parental R225X hiPSCs (referred to in the text and figures as Mutant or Mut) were cultured in parallel

707   throughout the whole gene editing procedure to provide a passage-matched control, and were re-banked

708   at passage 49 together with Corrected 1 and Corrected 2. These cells were confirmed to be euploid by

709   G-banding karyotyping. Mutant and Corrected hiPSCs to be used for derivation of hiPSC-CMs were

710   cultured between passage 50 to 60 before resorting to a new frozen stock.

711

712   **MEA**

713   Multi-electrode array (MEA) analyses were performed on hiPSC-CM monolayers at day 30 of

714   differentiation. hiPSC-CMs at day 21 of differentiation were seeded at a density of 5 x 10^4 cells per well

715   of 48-well MEA plates (CytoView MEA 48; Axion Byosystems) pre-coated with rhLaminin521 (2 µg/ml).

716   Cells were cultured in RPMI-B27 with media changes every other day. After 9 days (day 30 of

717   differentiation), cells were prepared for MEA analysis by changing the culture media to Tyrode's buffer

718   (140 mM NaCl, 5.4 mM KCl, 1.8 mM CaCl2, 1 mM MgCl2, 0.33 mM NaH$_2$PO$_4$, 5 mM D-glucose, and 10

719   mM HEPES; pH adjusted to 7.36) pre-warmed at 37 ºC. After 10 min of equilibration in Tyrode's buffer

720   at 37 ºC, MEA data were acquired for 5 min using the Maestro MEA system (Axion Biosystems) using

721   standard recording settings for spontaneous cardiac field potentials. Data acquisition and automated data

722   analysis was performed using Axis software, version 2.1. Standard acquisition settings have 130 × gain,

723 and record from 1 to 25 000 Hz, with a low-pass digital filter of 2 kHz for noise reduction. Automated data

724 analysis was focused on the 30 most stable beats within the recording period. The beat detection

725 threshold was 100 µV, and the field potential duration (FPD) detection utilized an inflection search

726 algorithm with the threshold set at 1.5 × noise to detect the T wave. The FPD was corrected for the beat

727 period (FPDc) according to the Fridericia's formula: FPDc = FPD / (beat period)$^{1/3}$ (Rast et al., 2016;

728 Asakura et al., 2015). Reported results for individual wells were calculated by averaging all of the

729 electrodes. In certain instances, poor signal quality and/or irregularity of field potential behavior prevented

730 the calculation of certain parameters (such as FPD). The presented data constitutes all recorded values

731 that could be reliably measured by the software based on automatic quality-control thresholds.

732

733 For pharmacological studies of P/Q- and L-type calcium current inhibition, Tyrode's buffer was

734 supplemented with 2 µM ω-Conotoxin MVIIC, 0.5 µM ω-Agatoxin TK, or 0.001-0.5 µM verapamil (all from

735 Tocris). hiPSC-CMs were incubated at 37 ºC for 20 min or 10 min (for ω-Conotoxin and ω-Agatoxin, or

736 verapamil, respectively) before MEA data acquisition.

737

738 **Whole cell patch clamp**

739 Whole-cell patch clamp recordings were obtained from individual hiPSC-CMs at day 30 of differentiation.

740 hiPSC-CMs at day 21 of differentiation were seeded at a density of 4.5 x 10^5 cells per well of 35-mm

741 glass-bottom FluoroDish with nanopatterned surfaces pre-coated with rhLaminin521 (2 µg/ml).

742 Anisotropically nanofabricated substrata (ANFS) with 800 nm topographic features were fabricated via

743 UV-assisted capillary force lithography as previously described (Macadangdang et al., 2015). First, liquid

744 polyurethane acrylate (PUA) prepolymer was drop dispensed onto a silicon master mold. A transparent

745 polyester film (PET) was then placed on top of the dispensed PUA. After exposure to UV radiation (λ =

746 250–400 nm), the film was peeled away from the silicon master, creating a PUA mold. A polyurethane-

747 based prepolymer (NOA76, Norland Products Inc.) was then drop dispensed onto standard glass

748 coverslips and the PUA mold was placed on top. The mold was then exposed to UV radiation for curing.

749 After curing, the PUA mold was peeled off, leaving behind an ANFS for cell culture. Dishes were sterilized

750 and activated by gas plasma treatment before coating with rhLaminin521. After 9 days, cells were

751 assayed by whole-cell patch clamp on the 37 °C heated stage of an inverted DIC microscope (Nikon)

752 connected to an EPC10 patch clamp amplifier and computer running Patchmaster software version

753 2x73.2 (HEKA). Cells on patterned coverslips were loaded onto the stage and bathed in Tyrode's buffer.

754 An intracellular recording solution (120 mM L-aspartic acid, 20 mM KCl, 5 mM NaCl, 1 mM MgCl2, 3 mM

755 Mg2+-ATP, 5 mM EGTA, and 10 mM HEPES) was used in conjunction with borosilicate glass patch

756 pipettes (World Precision Instruments) with a resistance in the range of 2–6 MΩ. Offset potentials were

23

757   nulled before formation of a gigaΩ seal and fast and slow capacitance was compensated for in all

758   recordings. Membrane potentials were corrected by subtraction of a 15 mV liquid junction potential

759   calculated by the HEKA software. Current injection was controlled by the software and used to hold

760   patched cells at an artificial resting membrane potential of -70 mV. Cells that required more than 100 pA

761   of current to achieve a -70 mV resting membrane potential were excluded from analysis as excessive

762   application of current was taken as indication of poor patch quality and/or membrane integrity. To

763   generate a single action potential, a 5 ms depolarizing current pulse of 50 nA was then applied and the

764   resulting voltage change recorded in current clamp mode. Action potential rise times were calculated as

765   the time taken to reach 90% maximum action potential amplitude from 10% of the maximum amplitude.

766   The exponential time constant (τ) was calculated from 90% to 10% repolarization of the action potential.

767   Action potential duration was calculated as the time delay between 10% of the maximum depolarization

768   and 90% repolarization from the maximum action potential amplitude. Gap-free recordings of

769   spontaneous cardiomyocyte activity were then collected for 30 seconds with 0 pA current injection to

770   provide a measure of the maximum diastolic membrane potential held by the cell without current input.

771

772   **Assessment of intracellular calcium fluxes**

773   Calcium fluxes were assessed in hiPSC-CM monolayers at day 30 of differentiation. hiPSC-CMs at day

774   21 of differentiation were seeded at a density of 5×10^5 cells per well of 6-well plate pre-coated with

775   rhLaminin521 (2 μg/ml). After 9 days, cells were prepared for imaging by incubation for 30 min at 37 ºC

776   with 1 μM Fluro-4, AM (ThermoFisher) diluted in culture media. Cells were rinsed in fresh media for 30

777   min at 37 ºC, and equilibrated in Tyrode's buffer pre-warmed at 37 ºC for 10 min. hiPSC-CMs were paced

778   at 1 Hz using a C-Dish for 6-well plate connected to a C-Pace EM cell stimulator (both from IonOptix)

779   providing biphasic field stimulation (pulses of 10 V/cm for 20 ms). Videos of Fluo-4 fluorescence

780   (excitation/emission of 494 and 516) were recorded at 20 frames per second (FPS) for at least 5

781   contractions using a Nikon Ti-E epi-fluorescent microscope with a 20x-objective and 1x coupler between

782   the microscope and Hamamatsu flash V3 camera. Videos were obtained for at least 20 random fields of

783   view. A custom Matlab program was used to define the region of interest (ROI, containing an individual

784   hiPSC-CM), threshold the Fluo-4 intensity based on the surrounding non-fluorescent background, and

785   track the average ROI_{Fluo-4} fluorescence (F) over time. The relaxation time constant, τ, was determined

786   by fitting the formula $F(t) = Ae^{-t/\tau} + B$ to the decay phase of the Fluo-4 transient profile, where t is time in

787   seconds and A and B are fitted constants.

24

CCQ analysis of cardiac contractility in hiPSC-CM monolayers

788
789 Contraction correlation quantification (CCQ) analysis was performed on hiPSC-CM monolayers at day

790 30 of differentiation. hiPSC-CMs at day 21 of differentiation were seeded at a density of 1 x 10^6 cells per

791 well of 6-well plate pre-coated with rhLaminin521 (2 μg/ml). After 9 days, cells were paced at 1 Hz as just

792 described for the measurement of calcium fluxes. Bright-field videos of at least ten contractions in multiple

793 random field of views were recorded at 30 fps using a Nikon TS100 microscope with a 20x-objective and

794 1x coupler between the microscope and a Canon VIXIA HF S20 camera. Videos were analyzed by CCQ

795 using a custom Matlab script, as previously described (Macadangdang et al., 2015). Briefly, this method

796 utilizes particle image velocimetry and digital image correlation algorithms to provide relevant contractile

797 endpoints from bright field video recordings. A reference video frame is divided into a grid of windows of

798 a set size. Each window is run through a correlation scheme with a second frame, providing the new

799 location for that window in the second frame. This displacement is converted into a vector map, which

800 provides contraction angles and, when spatially averaged, contraction magnitudes. The correlation

801 equation used provides a Gaussian correlation peak with a probabilistic nature that provides sub-pixel

802 accuracy.

803

Generation and biomechanical characterization of 3D-EHTs

804
805 3D engineered heart tissues (3D-EHTs) were generated and characterized with minor changes to a

806 previously described method (Leonard et al., 2018). Racks of polydimethylsiloxane (PDMS) posts were

807 fabricated by pouring uncured PDMS (Sylgard 184 mixed at a 1:10 curing agent to base ratio) into a

808 custom acrylic mold. Glass capillary tubes (1.1 mm diameter; Drummond) were cut to length and inserted

809 into the holes on one side of the mold before curing to render one post in each pair rigid. Post racks were

810 baked overnight at 65 °C before being peeled from the molds. Racks consisted of six pairs of posts that

811 were evenly spaced to fit along one row of a standard 24-well plate. Fabricated posts were 12.5 mm long

812 and 1.5 mm in diameter with a cap structure (2.0 mm diameter for the topmost 0.5 mm) to aide in the

813 attachment of 3D-EHTs. The center-to-center post spacing (corresponding to pre-compacted 3D-EHT

814 length) was 8 mm. Prior to casting 3D-EHTs, all 3D printed parts and PDMS posts were sterilized in a

815 UVO Cleaner (Jetlight, No. 342) for 7 min, submerged in 70% ethanol, and rinsed with sterile deionized

816 water. Rectangular 2% w/vol agarose/PBS casting troughs (12 mm in length, 4 mm in width, and ~4 mm

817 in depth) were generated in the bottom of 24-well plates by using custom 3D printed spacers (12 mm x

818 4 mm in cross section and 13 mm long) as negative molds. PDMS posts racks were positioned upside

819 down with one rigid-flexible post pair centered in each trough (leaving a 0.5 mm gap between the tip of

820 the post and the bottom of the casting trough). Each tissue consisted of a 97 μL fibrinogen-media solution

821 (89 μL of RPMI-B-27; 5.5 μL of 2X DMEM with 20% FBS; and 2.5 μL of 200 mg/mL bovine fibrinogen,

822   Sigma-Aldrich) containing 5×10^5 hiPSC-CMs and 5×10^4 supporting HS27a human bone marrow stromal

823   cells (ATCC), which was chilled and mixed with 3 µL of cold thrombin (at 100 U/mL, Sigma-Aldrich) just

824   before pipetting into the agarose casting troughs. The 3D-EHT mixtures were incubated for 90 min at 37

825   °C, at which point the fibrin gels were sufficiently polymerized around the posts to be lubricated in media

826   and transferred from the casting troughs into a 24-well plate with fresh 3D-EHT media (RPMI-B-27 with

827   penicillin/streptomycin, and 5 mg/mL aminocaproic acid, Sigma-Aldrich). 3D-EHTs were supplied with

828   2.5 mL/well of fresh 3D-EHT media three times per week.

829

830   *In situ* force measurements were performed after 4 weeks from 3D-EHT casting. In order to pace 3D-

831   EHTs, post racks were transferred to a custom-built 24-well plate with carbon electrodes connected

832   through an electrical stimulator (Astro Med Grass Stimulator, Model S88X) to provide biphasic field

833   stimulation (5 V/cm for 20 ms durations) during imaging (Leonard et al., 2018). 3D-EHTs were

834   equilibrated in Tyrode's buffer (containing 1.8 mM Ca^{2+}) pre-heated to 37 °C and paced at 1 Hz, which

835   was greater than the average spontaneous twitch frequency of the tissues. Videos of at least ten

836   contractions were recorded inside a 37 °C heated chamber using a monochrome CMOS camera

837   (Mightex, SMN-B050-U) with a board lens (The Imaging Source, TBL 8.4-2 5MP). The camera-lens

838   configuration allowed for a capture rate of 65 frames per second (FPS) with 8.3 µm/pixel resolution and

839   a field of view of 1536 × 400 pixels, which was sufficient to capture images of the whole 3D-EHT from

840   rigid to flexible post. A custom Matlab program was used to threshold the images and track the centroid

841   of the flexible post relative to the centroid of the rigid post. The twitch force profile, $F_{twitch}(t) = k_{post}*\Delta_{post}(t)$,

842   was calculated from the bending stiffness, k_{post}, and deflection of the flexible post, Δ_{post}, at all time points

843   (t), where k_{post} = 0.95 µN/µm was determined from beam bending theory using the dimensions of the

844   posts and taking the Young's modulus of PDMS to be 2.5 MPa (Sniadecki and Chen, 2007). The twitch

845   force and twitch kinetics were calculated from the twitch force profiles using a custom Matlab program.

846

847   **RT-qPCR**

848   Quantitative reverse-transcription PCR (RT-qPCR) was performed as previously described for 2D cell

849   monolayers (Fields et al., 2017) or 3D-EHTs (Leonard et al., 2018). 2D monolayers were lysed in RLT

850   buffer supplemented with 1% 2-Mercaptoethanol before RNA purification using the RNeasy Mini Kit

851   (QIAGEN) according to the manufacturer's instructions and including the on-column DNase digestion

852   step. cDNA was synthetized by reverse transcription of 500 ng of total RNA using M-MLV RT (Invitrogen)

853   and random hexamer priming according to the manufacturer's protocol and including RNase OUT

854   (Invitrogen). RT-qPCR was performed in technical duplicate with SYBR Select Master Mix (Applied

855   Biosystems) using 10 ng of cDNA and 400 nM forward and reverse primers. Reactions were run for 40

856   cycles on a 7900HT Fast Real-Time PCR System (Applied Biosystem, 4329001), all according to the

857   manufacturer's instructions, Gene expression relative to the housekeeping gene *RPLP0* was calculated

858   using the ∆Ct method as $2^{(Ct\ gene\ –\ Ct\ housekeeping)}$. Where indicated, gene expression was further normalized

859   to a control condition (which was set at the arbitrary value of 1). Primers were designed using PrimerBlast,

860   and confirmed to amplify a single product. A complete list can be found in Supplemental Table 7.

861

862   For 3D-EHTs, RNA was extracted using RNeasy Plus Micro Kit (QIAGEN) according to the

863   manufacturer's instructions except for the following modifications. Individual 3D-EHTs were pre-digested

864   using 2 mg/ml Proteinase K in 100 µl DPBS for 10 min at 56 °C in agitation. Cells were then lysed by

865   adding 350 µl of RLT Plus Buffer supplemented with 1% 2-Mercaptoethanol, and cleared through the

866   gDNA Eliminator Mini Spin Column. The RNA lysate was finally prepared for binding to the RNeasy

867   MinElute Spin Column by adding 250 µl of 200 proof ethanol. All subsequent steps were performed

868   according to the supplier's recommendations. 10 µl of eluted RNA (corresponding to 50-100 ng) were

869   subjected to reverse transcription, and 2 ng of cDNA were used as template for RT-qPCR, all as just

870   described for 2D monolayers.

871

872   **Western blot**

873   Protein lysates were obtained using ice-cold 1X RIPA buffer containing protease and phosphatase

874   inhibitors (Cell Signaling 9806), and freshly supplemented with 1 mM phenylmethylsulfonyl fluoride

875   (PMSF). After incubation for 30 min on ice, the lysate was clarified from insoluble material by

876   centrifugation at 16,000 g for 10 minutes at 4 °C. The protein concentration was assessed using the

877   Pierce BCA Protein Assay Kit (ThermoFisher) according to the manufacturer's instructions. After addition

878   of Laemmli Sample Buffer (Bio-Rad) to a final concentration of 1x, and 2-mercaptoethanol to a final

879   concentration of 2.5%, the samples were denatured by heating at 95 °C for 5 minutes. For electrophoretic

880   separation, 20 µg of protein for each sample was loaded onto 7.5% Mini-PROTEAN TGX Precast Protein

881   Gels (Bio-Rad) and run at 100V for 60 minutes using 1x Tris/Glycine/SDS running buffer (Bio-Rad).

882   Proteins were transferred onto Immobilion-P PVDF membranes (Millipore Sigma) by means of tank

883   blotting in 1X Tris/Glycine (Bio-Rad) supplemented with 20% methanol; transfer was performed at 100 V

884   for 60 minutes at 4 °C. Membranes were blocked in PBS supplemented with 0.1% Tween-20 (hereafter

885   PBST) and 4% Blotting-Grade Blocker (Bio-Rad) for 1 hr at room temperature. Primary antibody

886   incubation of whole membranes was performed overnight at 4 °C under agitation, and antibodies were

887   diluted in the same blocking buffer. The following antibodies were used: goat polyclonal anti-lamin A/C

888   (Santa Cruz sc-6215), 1:500 dilution; mouse monoclonal anti-TNNI (clone OTI8H8, Novus Biologicals

889   NBP2-46170), dilution 1:500; goat polyclonal anti-NKX2-5 (R&D Systems AF2444), dilution 1:500; goat

27

890   polyclonal anti-TBXT (R&D Systems AF2085), dilution 1:500; rabbit polyclonal anti-POU5F1 (Abcam

891   19857), dilution 1:1000; mouse monoclonal anti-GAPDH (clone 6C5, Abcam ab8245), dilution 1:2000.

892   Membranes were washed three times in PBST for 10 minutes at room temperature, incubated for 1 hr at

893   room temperature with species-appropriate HRP-conjugated secondary antibodies (ThermoFisher)

894   diluted 1:10,000 in blocking buffer, and washed three times in PBST for 10 minutes at room temperature.

895   Chemiluminescent reaction was initiated by incubation with SuperSignal West Pico PLUS

896   Chemiluminescent Substrate (ThermoFisher), and images were acquired using a ChemiDoc Imaging

897   System (Bio-Rad) in "high resolution" mode. Before re-probing with a new antibody, membranes were

898   treated with Restore Plus western blot stripping buffer (ThermoFisher), washed three times, and re-

899   blocked. Densitometric quantification of Western blots was performed using ImageJ, and protein

900   abundance estimation was normalized on the levels of GAPDH within each lysate.

901

902   **RNA-seq**

903   RNA sequencing (RNA-seq) was performed on 2-3 x 10^6 hiPSC-CMs at day 14 of differentiation on three

904   biological replicates (independent differentiations) per cell line. RNA-seq libraries were prepared from

905   100 ng of total RNA (obtained as described above for RT-qPCR) using the TruSeq Stranded Total RNA

906   LT Kit with Ribo-Zero H/M/R (all Illumina), according to the manufacturer's instructions. The analysis

907   RNA-seq libraries were paired-end sequenced on a Illumina NextSeq 500 in a high output run with 150

908   cycles (75 for each end), achieving approximately 40 million paired-end reads per sample. Reads were

909   mapped to hg38 using STAR (Dobin et al., 2013), and then quantified and processed through the

910   Cufflinks suite (Trapnell et al., 2012), all using default parameters. Differential expressed genes exhibited

911   a q-value < 0.05 for a pairwise comparison and were expressed at least 1 RPKM (read kilobase per

912   million mapped reads) in one time point. Hierarchical clustering was performed with the CummeRbund

913   suite in R. Ontology enrichment analysis was done using EnrichR (Chen et al., 2013). For comparision

914   with previously described RNA-seq data of hESC-CM differentiation (Fields et al., 2017), all datasets

915   were collectively re-normalized and -quantified using Cufflinks. Principal component analysis (PCA) was

916   performed using the R function "prcomp".

917

918   *In situ* **DNase Hi-C**

919   Genome-wide chromosome conformation capture based on *in situ* proximity ligation of DNase I-digested

920   nuclei (DNase Hi-C) was performed with minor modifications of a previously described method (Ramani

921   et al., 2016; Fields et al., 2017). The assay was performed on ~2 x 10^6 hiPSC-CMs at day 14 of

922   differentiation on two biological replicates (independent differentiations) per cell line. Unless otherwise

923   indicated, all molecular biology reagents were from ThermoFisher and reactions were performed at room

924   temperature (RT). Cells were fixed in the dish with fresh RPMI-1640 supplemented with 2% formaldehyde

925   while in gentle orbital rotation for 10 min, and subsequently quenched with 25 mM Glycine for 5 min at

926   room temperature followed by 15 min at 4 °C. Cells were then treated with 0.05% Trypsin for 10 min at

927   37 °C, rinsed in RPMI-1640 with 10% FBS, and scraped off the plate. Cells were washed once with PBS,

928   flash frozen in liquid nitrogen, and stored at -80 °C. After rapid thawing, samples were resuspended in

929   500 µL of ice-cold cell lysis buffer (10 mM Tris-HCl pH 8.0, 10 mM NaCl, 0.5% Igepal CA-630,

930   supplemented with the protease inhibitor cocktail from Sigma-Aldrich), incubated for 20 min on ice, and

931   dounce-homogenized 60-80 times with a tight pestle. Extracted nuclei were centrifuged at 2,500 g for 1

932   min at RT (standard spinning protocol), resuspended in 300 µL 0.5x DNase I digestion buffer with 0.2%

933   SDS and 20 mM MnCl2, and incubated at 37 °C for 60 min with periodic gentle vortexing. Then, 300 µL

934   0.5x DNase I digestion buffer with 2% Triton X-100, 20 mM MnCl2, and 0.4 µg/µL RNase A were added

935   and incubated for another 10 min. Chromatin was finally digested with 7 U of DNase I during a 7 min

936   incubation at RT. The reaction was stopped with 30 µL of 0.5M EDTA and 15 µL 10% SDS. The efficiency

937   of DNase I digestion was confirmed by comparing the DNA shearing patterns of small samples of

938   undigested and digested nuclei using a 6% PAGE gel (following proteinase K digestion). Nuclei were

939   spun down and resuspended in 150 µl RNase and DNase-free water. 300 µl of AMPure XP beads

940   (Beckman) were added to irreversibly bind nuclei; going forward nuclei were therefore cleaned up by

941   magnetic purification. *In situ* reactions were performed first for end repair (15 U of T4 DNA Polymerase

942   and 30 U of Klenow Fragment for 1 hr at RT) and dA-tailing (75 U of Klenow exo-minus for 1 hr at 37 °C),

943   each in 200 µL, and followed by inactivation with 5 µL of 10% SDS and cleanup. Nuclei were then

944   subjected to overnight ligation of custom T- and blunt-bridge biotin-tagged adapters (each at 8 µM;

945   sequences detailed in Ramani et al., 2016) using 25 U of T4 DNA ligase and 5% polyethylene glycol

946   (PEG) in a 100 µl reaction incubated at 16 °C. The reaction was stopped with 5 µL of 10% SDS, and

947   nuclei were washed twice with AMPure buffer (20% PEG in 2.5 M NaCl) followed by 2 washes with 80%

948   ethanol to remove un-ligated adapter. Nuclei were then treated for 1 hr at 37 °C with 100 U of T4 PNK in

949   a 100 µL reaction to phosphorylate the adapters. Proximity ligation of DNA ends was performed for 4

950   hours at RT using 30 U of T4 DNA ligase in a 1 mL reaction maintained in gentle agitation. Nuclei were

951   resuspended in 1x NEBuffer 2 (New England Biolabs) with 1% SDS, and digested with 800 µg of

952   Proteinase K overnight at 62 °C. DNA was precipitated by adding 60 µg glycogen, 50 µL 3M Na-acetate

953   (ph5.2) and 500 µL isopropanol followed by incubation for 2 hours at -80 °C and centrifugation at 16,000

954   g for 30 min at 4 °C. DNA was resuspended in 100 µL water and purified with 100 µL AMPure beads

955   according to the manufacturer's instructions, and resuspended in 100 µL elution buffer (EB; 10 mM Tris-

956   HCl pH 8.5). Biotin pull-down was performed on the purified DNA to isolate ligation products containing

957   the biotin adapters. 100 µL Myone C1 beads were mixed with the DNA for 30 min at RT under gentle

958   rotation. Samples were washed 4 times with B&W buffer (5 mM Tris-HCl pH 8.0, 0.5 mM EDTA, 1 M

959   NaCl, 0.05% Tween-20), and twice with EB. DNA was then treated on the beads to perform end-repair

960   (200 µL reaction with the Fast DNA End Repair Kit for 10 min at 18 °C) and dA-Tailing (50 µL reaction

961   with 25 U of Klenow exo-minus in NEBuffer 2 and 1.2 mM dATP for 30 min at 37 °C). Custom Y-adapters

962   for Illumina sequencing (each at 2 µM; sequences detailed in Ramani et al., 2016) were then ligated

963   using 20 U of T4 DNA ligase for 1 hour at RT in a 50 µL reaction using the Rapid Ligation Buffer. Beads

964   were washed 4 times with B&W buffer and twice with EB after each of these reactions. Finally, libraries

965   were amplified by 12 PCR cycles with Kapa HiFi ReadyStart Master Mix with custom barcode-containing

966   primers (sequences detailed in Ramani et al., 2016). Libraries were purified with 0.8x Ampure XP beads

967   according to the manufacturer's instructions, quantified with a Qubit and the DNA high-sensitivity reagent,

968   and pooled at equimolar ratios in preparation for next-generation sequencing. Samples were paired-end

969   sequenced on three runs with an Illumina NextSeq 500 at high output with 150 cycles (75 for each end),

970   resulting in approximately 150 M paired-end reads per sample.

971

972   **Hi-C data analysis**

973   Fastq files were mapped to the hg38 genome using BWA-MEM with default parameters, mapping each

974   end of the read pairs individually. The mapped files were processed through HiC-Pro (Servant et al.,

975   2015), filtering for MAPQ score greater than 30 and excluding pairs less than 1 Kb apart, to generate

976   valid pairs and ICE balanced matrices at 500 Kb resolution. Hi-C QC metrics from HiC-Pro are reported

977   in Supplemental Table 3. Samples were clustered based on HiC-Rep scores calculated using a resolution

978   of 500 Kb with a max distance of 5 Mb and h = 1 (Yang et al., 2017). Hi-C contact matrix heatmaps for

979   *cis* or *trans* interactions were generated with Cooler (https://github.com/mirnylab/cooler) using default

980   parameters and logarithmic interaction probabilities, without diagonals. A/B compartmentalization was

981   computed by eigenvalue decomposition of the contact maps using HOMER (Heinz et al., 2010) with 500

982   Kb resolution and no additional windowing (super-resolution also set at 500 Kb). The sign of the first

983   eigenvector (PC1) was selected based on the expression ~5000 genes constitutively expressed across

984   hESC-CM differentiation (Fields et al., 2017), so that positive and negative values indicate A and B

985   compartmentalization, respectively. Saddle plots of inter-compartment interaction enrichment were

986   generated by assigning each genomic bin to its corresponding percentile value based on PC1, and

987   dividing the genome into 10 deciles. Each interaction was normalized to the average score at the

988   corresponding distance (for *cis* interactions) or to the average of all contacts (for *trans* interactions), and

989   assigned to a pair of deciles based on the PC1 scores of the two bins. The data was plotted in heatmaps

990   representing the $\log_2$ average value for pairs of deciles, while the change between mutant and corrected

991   hiPSC-CMs is the $\log_2$ value of the difference in such values. To calculate the interaction probability at

992   varying genomic distances based on compartmentalization, each interaction was assigned to A-A, B-B,

993   or A-B based on the pairs of bins involved, and then the average interaction score for a given distance

994   was normalized to the average interaction score for all pairs of contacts at that distance. The data was

995   plotted on a logarithmic scale and loess-smoothed using the R function "geom_smooth". Visualization of

996   sample similarity by PC1 scores was performed with the R function "prcomp". Gene tracks were

997   generated using IGV (Thorvaldsdóttir et al., 2013). Changes in A/B compartmentalization were

998   determined by a one-way ANOVA of PC1 scores across the two replicates for the three cell lines, using

999   a significance cutoff of p-value < 0.05 combined by the need for the average PC1 to change sign across

1000   at least one pair of condition. Consistent changes in A/B compartmentalization were further selected if

1001   the average PC1 score for mutant hiPSC-CMs changed sign compared the average PC1 score of each

1002   corrected hiPSC-CMs.

1003

Statistical analyses

1005   Unless specifically described elsewhere in the methods, all statistical analyses were performed using

1006   Prism 7 (GraphPad). The type and number of replicates, the statistics plotted, the statistical test used,

1007   and the test results are described in the figure legends. All statistical tests employed were two-tailed. No

1008   experimental samples were excluded from the statistical analyses. Sample size was not pre-determined

1009   through power calculations, and no randomization or investigator blinding approaches were implemented

1010   during the experiments and data analyses. When a representative experiment is reported, this

1011   exemplifies the results obtained in at least two independent biological replications.

1012

Data and code availability

1014   Hi-C and RNA-seq data is available on Gene Expression Omnibus accession number GSE126460.

1015   Custom code for Hi-C analyses was previously described (Fields et al., 2017) and is available on github

1016   (https://github.com/pfields8/Fields_et_al_2018/). All other raw data and custom code is available from

1017   the corresponding author upon reasonable request.

1018

Supplemental material

1020   The Supplemental material linked to this article includes Supplemental Figures 1 to 4 and their matching

1021   Figure Legends (presented in the same document), Supplemental Tables 1 to 5 (presented as individual

1022   files), Supplemental Tables 6 and 7 (presented in the same document as the Supplemental Figures), and

1023   Supplemental Videos 1 to 8 (presented as individual files).

Acknowledgments

Author contributions

A.B. lead methodology, investigation, formal analysis, data curation, visualization, writing - original draft, and writing - review and editing; supporting conceptualization. P.F. supporting software, and formal analysis (Hi-C and RNA-seq); supporting writing – review and editing. A.S.T.S: supporting investigation and formal analysis (patch clamp); supporting writing – review and editing. A.L.: supporting methodology, software, and formal analysis (3D-EHT contractility). K.B: supporting software and formal analysis (Fluo-4). H-F.T: supporting resources (hiPSCs). N.J.S, D-H.K., J.S. W.S.N: supporting supervision, funding acquisition, and resources. L.P.: supporting supervision, project administration, and writing – review and editing. C.E.M. lead conceptualization, supervision, project administration, resources, and writing – review & editing. All authors have read, commented, and approved the final manuscript.

References

Adams, M.E., I.M. Mintz, M.D. Reily, V. Thanabal, and B.P. Bean. 1993. Structure and properties of omega-agatoxin IVB, a new antagonist of P-type calcium channels. *Mol. Pharmacol.* 44:681–688.

Adriaens, C., L.A. Serebryannyy, M. Feric, A. Schibler, K.J. Meaburn, N. Kubben, P. Trzaskoma, S. Shachar, S. Vidak, E.H. Finn, V. Sood, G. Pegoraro, and T. Misteli. 2018. Blank spots on the map: some current questions on nuclear organization and genome architecture. *Histochem. Cell Biol.* 150:579–592. doi:10.1007/s00418-018-1726-1.

Akinrinade, O., L. Ollila, S. Vattulainen, J. Tallila, M. Gentile, P. Salmenperä, H. Koillinen, M. Kaartinen, M.S. Nieminen, S. Myllykangas, T.-P. Alastalo, J.W. Koskenvuo, and T. Heliö. 2015. Genetics and genotype–phenotype correlations in Finnish patients with dilated cardiomyopathy. *Eur. Heart J.* 36:2327–2337. doi:10.1093/eurheartj/ehv253.

Amendola, M., and B. van Steensel. 2015. Nuclear lamins are not required for lamina-associated domain organization in mouse embryonic stem cells. *EMBO Rep.* 16:610–7. doi:10.15252/embr.201439789.

Amin, A.S., H.L. Tan, and A.A.M. Wilde. 2010. Cardiac ion channels in health and disease. *Hear. Rhythm*. 7:117–126. doi:10.1016/j.hrthm.2009.08.005.

Arimura, T., A. Helbling-Leclerc, C. Massart, S. Varnous, F. Niel, E. Lacène, Y. Fromes, M. Toussaint, A.-M. Mura, D.I. Keller, H. Amthor, R. Isnard, M. Malissen, K. Schwartz, and G. Bonne. 2005. Mouse model carrying H222P- Lmna mutation develops muscular dystrophy and dilated cardiomyopathy similar to human striated muscle laminopathies. *Hum. Mol. Genet.* 14:155–169. doi:10.1093/hmg/ddi017.

Asakura, K., S. Hayashi, A. Ojima, T. Taniguchi, N. Miyamoto, C. Nakamori, C. Nagasawa, T. Kitamura, T. Osada, Y. Honda, C. Kasai, H. Ando, Y. Kanda, Y. Sekino, and K. Sawada. 2015. Improvement of acquisition and analysis methods in multi-electrode array experiments with iPS cell-derived cardiomyocytes. *J. Pharmacol. Toxicol. Methods*. 75:17–26. doi:10.1016/j.vascn.2015.04.002.

Awasthi, A., B. Ramachandran, S. Ahmed, E. Benito, Y. Shinoda, N. Nitzan, A. Heukamp, S. Rannio, H. Martens, J. Barth, K. Burk, Y.T. Wang, A. Fischer, and C. Dean. 2018. Synaptotagmin-3 drives AMPA receptor endocytosis, depression of synapse strength, and forgetting. *Science*. 363:eaav1483. doi:10.1126/science.aav1483.

Bellin, M., S. Casini, R.P. Davis, C. D'Aniello, J. Haas, D. Ward-van Oostwaard, L.G.J. Tertoolen, C.B. Jung, D.A. Elliott, A. Welling, K.-L. Laugwitz, A. Moretti, and C.L. Mummery. 2013. Isogenic human pluripotent stem cell pairs reveal the role of a KCNH2 mutation in long-QT syndrome. *EMBO J.* 32:3161–3175. doi:10.1038/emboj.2013.240.

Van Berlo, J.H., W.G. De Voogt, A.J. Van Der Kooi, J.P. Van Tintelen, G. Bonne, R. Ben Yaou, D. Duboc, T. Rossenbacker, H. Heidbüchel, M. De Visser, H.J.G.M. Crijns, and Y.M. Pinto. 2005. Meta-analysis of clinical characteristics of 299 carriers of LMNA gene mutations: Do lamin A/C mutations portend a high risk of sudden death? *J. Mol. Med.* 83:79–83. doi:10.1007/s00109-004-0589-1.

Bertrand, A.T., K. Chikhaoui, R. Ben Yaou, and G. Bonne. 2011. Clinical and genetic heterogeneity in laminopathies. *Biochem. Soc. Trans.* 39:1687–92. doi:10.1042/BST20110670.

Bodi, I., G. Mikala, S.E. Koch, S.A. Akhter, and A. Schwartz. 2005. The L-type calcium channel in the heart: the beat goes on. *J. Clin. Invest.* 115:3306–3317. doi:10.1172/JCI27167.

Bolzer, A., G. Kreth, I. Solovei, D. Koehler, K. Saracoglu, C. Fauth, S. Müller, R. Eils, C. Cremer, M.R. Speicher, and T. Cremer. 2005. Three-dimensional maps of all chromosomes in human male fibroblast nuclei and prometaphase rosettes. *PLoS Biol.* 3:e157. doi:10.1371/journal.pbio.0030157.

Bonne, G., K. Schwartz, M.R. Di Barletta, S. Varnous, H.-M. Bécane, E.-H. Hammouda, L. Merlini, F. Muntoni, C.R. Greenberg, F. Gary, J.-A. Urtizberea, D. Duboc, M. Fardeau, and D. Toniolo. 1999. Mutations in the gene encoding lamin A/C cause autosomal dominant Emery-Dreifuss muscular dystrophy. *Nat. Genet.* 21:285–288. doi:10.1038/6799.

Branco, M.R., and A. Pombo. 2006. Intermingling of chromosome territories in interphase suggests role in translocations and transcription-dependent associations. *PLoS Biol.* 4:e138. doi:10.1371/journal.pbio.0040138.

Buchwalter, A., J.M. Kaneshiro, and M.W. Hetzer. 2018. Coaching from the sidelines: the nuclear periphery in genome regulation. *Nat. Rev. Genet.* 20:39–50. doi:10.1038/s41576-018-0063-5.

Burridge, P.W., E. Matsa, P. Shukla, Z.C. Lin, J.M. Churko, A.D. Ebert, F. Lan, S. Diecke, B. Huber, N.M. Mordwinkin, J.R. Plews, O.J. Abilez, B. Cui, J.D. Gold, and J.C. Wu. 2014. Chemically defined generation of human cardiomyocytes. *Nat. Methods*. 11:855–60. doi:10.1038/nmeth.2999.

Capell, B.C., and F.S. Collins. 2006. Human laminopathies: nuclei gone genetically awry. *Nat. Rev. Genet.* 7:940–952. doi:10.1038/nrg1906.

Captur, G., E. Arbustini, G. Bonne, P. Syrris, K. Mills, K. Wahbi, S.A. Mohiddin, W.J. McKenna, S. Pettit, C.Y. Ho, A. Muchir, P. Gissen, P.M. Elliott, and J.C. Moon. 2018. Lamin and the heart. *Heart*. 104:468–479. doi:10.1136/heartjnl-2017-312338.

Carson, D., M. Hnilova, X. Yang, C.L. Nemeth, J.H. Tsui, A.S.T. Smith, A. Jiao, M. Regnier, C.E. Murry, C. Tamerler, and D.-H. Kim. 2016. Nanotopography-Induced Structural Anisotropy and Sarcomere Development in Human Cardiomyocytes Derived from Induced Pluripotent Stem Cells. *ACS Appl. Mater. Interfaces*. 8:21923–32. doi:10.1021/acsami.5b11671.

Catterall, W. a, E. Perez-Reyes, T.P. Snutch, and J. Striessnig. 2005. International Union of Pharmacology. XLVIII. Nomenclature and structure-function relationships of voltage-gated calcium channels. *Pharmacol. Rev.* 57:411–425. doi:10.1124/pr.57.4.5.units.

Cattin, M.-E., A. Muchir, and G. Bonne. 2013. "State-of-the-heart" of cardiac laminopathies. *Curr Opin Cardiol*. 28:297–304. doi:10.1097/HCO.0b013e32835f0c79.

Chen, E.Y., C.M. Tan, Y. Kou, Q. Duan, Z. Wang, G.V. Meirelles, N.R. Clark, and A. Ma'ayan. 2013. Enrichr: interactive and collaborative HTML5 gene list enrichment analysis tool. *BMC Bioinformatics*. 14:128. doi:10.1186/1471-2105-14-128.

Chen, W. V., and T. Maniatis. 2013. Clustered protocadherins. *Development*. 140:3297–3302. doi:10.1242/dev.090621.

Choi, J.C., A. Muchir, W. Wu, S. Iwata, S. Homma, J.P. Morrow, and H.J. Worman. 2012. Temsirolimus activates autophagy and ameliorates cardiomyopathy caused by lamin A/C gene mutation. *Sci. Transl. Med.* 4:144ra102.

1116   doi:10.1126/scitranslmed.3003875.

1117 Constantinescu, D., H.L. Gray, P.J. Sammak, G.P. Schatten, and A.B. Csoka. 2006. Lamin A/C expression is a marker of mouse
1118   and human embryonic stem cell differentiation. *Stem Cells*. 24:177–185. doi:10.1634/stemcells.2004-0159.

1119 Dekker, J., A.S. Belmont, M. Guttman, V.O. Leshyk, J.T. Lis, S. Lomvardas, L.A. Mirny, C.C. O'Shea, P.J. Park, B. Ren, J.C.
1120   Ritland Politz, J. Shendure, and S. Zhong. 2017. The 4D nucleome project. *Nature*. 549:219–226.
1121   doi:10.1038/nature23884.

1122 Dixon, J.R., I. Jung, S. Selvaraj, Y. Shen, J.E. Antosiewicz-Bourget, A.Y. Lee, Z. Ye, A. Kim, N. Rajagopal, W. Xie, Y. Diao, J.
1123   Liang, H. Zhao, V. V. Lobanenkov, J.R. Ecker, J.A. Thomson, and B. Ren. 2015. Chromatin architecture reorganization
1124   during stem cell differentiation. *Nature*. 518:331–336. doi:10.1038/nature14222.

1125 Dixon, J.R., S. Selvaraj, F. Yue, A. Kim, Y. Li, Y. Shen, M. Hu, J.S. Liu, and B. Ren. 2012. Topological domains in mammalian
1126   genomes identified by analysis of chromatin interactions. *Nature*. 485:376–380. doi:10.1038/nature11082.

1127 Dobin, A., C.A. Davis, F. Schlesinger, J. Drenkow, C. Zaleski, S. Jha, P. Batut, M. Chaisson, and T.R. Gingeras. 2013. STAR:
1128   ultrafast universal RNA-seq aligner. *Bioinformatics*. 29:15–21. doi:10.1093/bioinformatics/bts635.

1129 Dobrzynska, A., S. Gonzalo, C. Shanahan, and P. Askjaer. 2016. The nuclear lamina in health and disease. *Nucleus*. 7:233–
1130   248. doi:10.1080/19491034.2016.1183848.

1131 Eisner, D.A., J.L. Caldwell, K. Kistamás, and A.W. Trafford. 2017. Calcium and Excitation-Contraction Coupling in the Heart.
1132   *Circ. Res.* 121:181–195. doi:10.1161/CIRCRESAHA.117.310230.

1133 Fields, P.A., V. Ramani, G. Bonora, G.G. Yardimci, A. Bertero, H. Reinecke, L. Pabon, W.S. Noble, J. Shendure, and C. Murry.
1134   2017. Dynamic reorganization of nuclear architecture during human cardiogenesis. *bioRxiv*. 222877. doi:10.1101/222877.

1135 Fontana, M., A. Barison, N. Botto, L. Panchetti, G. Ricci, M. Milanesi, R. Poletti, V. Positano, G. Siciliano, C. Passino, M.
1136   Lombardi, M. Emdin, and P.G. Masci. 2013. CMR-Verified Interstitial Myocardial Fibrosis as a Marker of Subclinical
1137   Cardiac Involvement in LMNA Mutation Carriers. *JACC Cardiovasc. Imaging*. 6:124–126. doi:10.1016/j.jcmg.2012.06.013.

1138 Fraser, J., C. Ferrai, A.M. Chiariello, M. Schueler, T. Rito, G. Laudanno, M. Barbieri, B.L. Moore, D.C. Kraemer, S. Aitken, S.Q.
1139   Xie, K.J. Morris, M. Itoh, H. Kawaji, I. Jaeger, Y. Hayashizaki, P. Carninci, A.R. Forrest, C.A. Semple, J. Dostie, A. Pombo,
1140   and M. Nicodemi. 2015. Hierarchical folding and reorganization of chromosomes are linked to transcriptional changes in
1141   cellular differentiation. *Mol. Syst. Biol.* 11:852–852. doi:10.15252/msb.20156492.

1142 Guelen, L., L. Pagie, E. Brasset, W. Meuleman, M.B. Faza, W. Talhout, B.H. Eussen, A. de Klein, L. Wessels, W. de Laat, and
1143   B. van Steensel. 2008. Domain organization of human chromosomes revealed by mapping of nuclear lamina interactions.
1144   *Nature*. 453:948–51. doi:10.1038/nature06947.

1145 Haas, J., K.S. Frese, B. Peil, W. Kloos, A. Keller, R. Nietsch, Z. Feng, S. Müller, E. Kayvanpour, B. Vogel, F. Sedaghat-
1146   Hamedani, W.K. Lim, X. Zhao, D. Fradkin, D. Köhler, S. Fischer, J. Franke, S. Marquart, I. Barb, D.T. Li, A. Amr, P.
1147   Ehlermann, D. Mereles, T. Weis, S. Hassel, A. Kremer, V. King, E. Wirsz, R. Isnard, M. Komajda, A. Serio, M. Grasso, P.
1148   Syrris, E. Wicks, V. Plagnol, L. Lopes, T. Gadgaard, H. Eiskjær, M. Jørgensen, D. Garcia-Giustiniani, M. Ortiz-Genga,
1149   M.G. Crespo-Leiro, R.H.L.D. Deprez, I. Christiaans, I.A. Van Rijsingen, A.A. Wilde, A. Waldenstrom, M. Bolognesi, R.
1150   Bellazzi, S. Mörner, J.L. Bermejo, L. Monserrat, E. Villard, J. Mogensen, Y.M. Pinto, P. Charron, P. Elliott, E. Arbustini,
1151   H.A. Katus, and B. Meder. 2015. Atlas of the clinical genetics of human dilated cardiomyopathy. *Eur. Heart J.* 36:1123–
1152   1135. doi:10.1093/eurheartj/ehu301.

1153 Harr, J.C., T.R. Luperchio, X. Wong, E. Cohen, S.J. Wheelan, and K.L. Reddy. 2015. Directed targeting of chromatin to the
1154   nuclear lamina is mediated by chromatin state and A-type lamins. *J. Cell Biol.* 208:33–52. doi:10.1083/jcb.201405110.

1155 Hasselberg, N.E., T.F. Haland, J. Saberniak, P.H. Brekke, K.E. Berge, T.P. Leren, T. Edvardsen, and K.H. Haugaa. 2018. Lamin
1156   A/C cardiomyopathy: Young onset, high penetrance, and frequent need for heart transplantation. *Eur. Heart J.* 39:853–
1157   860. doi:10.1093/eurheartj/ehx596.

1158 Hayashi, S., and M. Takeichi. 2015. Emerging roles of protocadherins: from self-avoidance to enhancement of motility. *J. Cell
1159   Sci.* 128:1455–1464. doi:10.1242/jcs.166306.

1160 Heinz, S., C. Benner, N. Spann, E. Bertolino, Y.C. Lin, P. Laslo, J.X. Cheng, C. Murre, H. Singh, and C.K. Glass. 2010. Simple
1161   combinations of lineage-determining transcription factors prime cis-regulatory elements required for macrophage and B
1162   cell identities. *Mol. Cell*. 38:576–89. doi:10.1016/j.molcel.2010.05.004.

1163 Ho, J.C.Y., T. Zhou, W.H. Lai, Y. Huang, Y.C. Chan, X. Li, N.L.Y. Wong, Y. Li, K.W. Au, D. Guo, J. Xu, C.W. Siu, D. Pei, H.F.
1164   Tse, and M.A. Esteban. 2011. Generation of induced pluripotent stem cell lines from 3 distinct laminopathies bearing
1165   heterogeneous mutations in lamin A/C. *Aging*. 3:380–390. doi:10.18632/aging.100277.

1166 Imakaev, M., G. Fudenberg, R.P. McCord, N. Naumova, A. Goloborodko, B.R. Lajoie, J. Dekker, and L.A. Mirny. 2012. Iterative
1167   correction of Hi-C data reveals hallmarks of chromosome organization. *Nat. Methods*. 9:999–1003.
1168   doi:10.1038/nmeth.2148.

1169 Jakobs, P.M., E.L. Hanson, K.A. Crispell, W. Toy, H. Keegan, K. Schilling, T.B. Icenogle, M. Litt, and R.E. Hershberger. 2001.

1170   Novel lamin A/C mutations in two families with dilated cardiomyopathy and conduction system disease. *J. Card. Fail.*
1171   7:249–256. doi:10.1054/jcaf.2001.26339.

1172 Kalhor, R., H. Tjong, N. Jayathilaka, F. Alber, and L. Chen. 2012. Genome architectures revealed by tethered chromosome
1173   conformation capture and population-based modeling. *Nat. Biotechnol.* 30:90–98. doi:10.1038/nbt.2057.

1174 Katainen, R., K. Dave, E. Pitkänen, K. Palin, T. Kivioja, N. Välimäki, A.E. Gylfe, H. Ristolainen, U.A. Hänninen, T. Cajuso, J.
1175   Kondelin, T. Tanskanen, J.-P. Mecklin, H. Järvinen, L. Renkonen-Sinisalo, A. Lepistö, E. Kaasinen, O. Kilpivaara, S.
1176   Tuupanen, M. Enge, J. Taipale, and L.A. Aaltonen. 2015. CTCF/cohesin-binding sites are frequently mutated in cancer.
1177   *Nat. Genet.* 47:818–21. doi:10.1038/ng.3335.

1178 Kind, J., L. Pagie, S.S. De Vries, L. Nahidiazar, S.S. Dey, M. Bienko, Y. Zhan, B. Lajoie, C.A. De Graaf, M. Amendola, G.
1179   Fudenberg, M. Imakaev, L.A. Mirny, K. Jalink, J. Dekker, A. Van Oudenaarden, and B. Van Steensel. 2015. Genome-wide
1180   Maps of Nuclear Lamina Interactions in Single Human Cells. *Cell.* 163:134–147. doi:10.1016/j.cell.2015.08.040.

1181 Kodo, K., S.-G. Ong, F. Jahanbani, V. Termglinchan, K. Hirono, K. InanlooRahatloo, A.D. Ebert, P. Shukla, O.J. Abilez, J.M.
1182   Churko, I. Karakikes, G. Jung, F. Ichida, S.M. Wu, M.P. Snyder, D. Bernstein, and J.C. Wu. 2016. iPSC-derived
1183   cardiomyocytes reveal abnormal TGF-β signalling in left ventricular non-compaction cardiomyopathy. *Nat. Cell Biol.*
1184   18:1031–42. doi:10.1038/ncb3411.

1185 Krumm, A., and Z. Duan. 2018. Understanding the 3D genome: Emerging impacts on human disease. *Semin. Cell Dev. Biol.*
1186   doi:10.1016/j.semcdb.2018.07.004.

1187 Kumar, S., S.H. Baldinger, E. Gandjbakhch, P. Maury, J.M. Sellal, A.F.A. Androulakis, X. Waintraub, P. Charron, A. Rollin, P.
1188   Richard, W.G. Stevenson, C.J. Macintyre, C.Y. Ho, T. Thompson, J.K. Vohra, J.M. Kalman, K. Zeppenfeld, F. Sacher,
1189   U.B. Tedrow, and N.K. Lakdawala. 2016. Long-Term Arrhythmic and Nonarrhythmic Outcomes of Lamin A/C Mutation
1190   Carriers. *J. Am. Coll. Cardiol.* 68:2299–2307. doi:10.1016/j.jacc.2016.08.058.

1191 Lee, P.J.H., D. Rudenko, M.A. Kuliszewski, C. Liao, M.G. Kabir, K.A. Connelly, and H. Leong-Poi. 2014. Survivin gene therapy
1192   attenuates left ventricular systolic dysfunction in doxorubicin cardiomyopathy by reducing apoptosis and fibrosis.
1193   *Cardiovasc. Res.* 101:423–433. doi:10.1093/cvr/cvu001.

1194 Lee, Y., Y. Lau, Z. Cai, W. Lai, L. Wong, H. Tse, K. Ng, and C. Siu. 2017. Modeling Treatment Response for Lamin A/C Related
1195   Dilated Cardiomyopathy in Human Induced Pluripotent Stem Cells. *J. Am. Heart Assoc.* 6:e005677.
1196   doi:10.1161/JAHA.117.005677.

1197 Leonard, A., A. Bertero, J.D. Powers, K.M. Beussman, S. Bhandari, M. Regnier, C.E. Murry, and N.J. Sniadecki. 2018. Afterload
1198   promotes maturation of human induced pluripotent stem cell derived cardiomyocytes in engineered heart tissues. *J. Mol.*
1199   *Cell. Cardiol.* 118:147–158. doi:10.1016/j.yjmcc.2018.03.016.

1200 Lieberman-Aiden, E., N.L. van Berkum, L. Williams, M. Imakaev, T. Ragoczy, A. Telling, I. Amit, B.R. Lajoie, P.J. Sabo, M.O.
1201   Dorschner, R. Sandstrom, B. Bernstein, M.A. Bender, M. Groudine, A. Gnirke, J. Stamatoyannopoulos, L.A. Mirny, E.S.
1202   Lander, and J. Dekker. 2009. Comprehensive mapping of long-range interactions reveals folding principles of the human
1203   genome. *Science.* 326:289–93. doi:10.1126/science.1181369.

1204 Liu, G.-H., B.Z. Barkho, S. Ruiz, D. Diep, J. Qu, S.-L. Yang, A.D. Panopoulos, K. Suzuki, L. Kurian, C. Walsh, J. Thompson, S.
1205   Boue, H.L. Fung, I. Sancho-Martinez, K. Zhang, J.Y. III, and J.C.I. Belmonte. 2011. Recapitulation of premature ageing
1206   with iPSCs from Hutchinson–Gilford progeria syndrome. *Nature.* 472:221–225. doi:10.1038/nature09879.

1207 Luperchio, T.R., M.E.G. Sauria, X. Wong, M. Gaillard, P. Tsang, and K. Pekrun. 2017. Chromosome Conformation Paints Reveal
1208   the Role of Lamina Association in Genome Organization and Regulation. *bioRxiv.* doi:10.1101/122226.

1209 Lupiáñez, D.G., K. Kraft, V. Heinrich, P. Krawitz, F. Brancati, E. Klopocki, D. Horn, H. Kayserili, J.M. Opitz, R. Laxova, F. Santos-
1210   Simarro, B. Gilbert-Dussardier, L. Wittler, M. Borschiwer, S.A. Haas, M. Osterwalder, M. Franke, B. Timmermann, J. Hecht,
1211   M. Spielmann, A. Visel, and S. Mundlos. 2015. Disruptions of topological chromatin domains cause pathogenic rewiring
1212   of gene-enhancer interactions. *Cell.* 161:1012–1025. doi:10.1016/j.cell.2015.04.004.

1213 Macadangdang, J., X. Guan, A.S.T. Smith, R. Lucero, S. Czerniecki, M.K. Childers, D.L. Mack, and D.-H. Kim. 2015.
1214   Nanopatterned Human iPSC-based Model of a Dystrophin-Null Cardiomyopathic Phenotype. *Cell. Mol. Bioeng.* 8:320–
1215   332. doi:10.1007/s12195-015-0413-8.

1216 Maruo, T., K. Mandai, M. Miyata, S. Sakakibara, S. Wang, K. Sai, Y. Itoh, A. Kaito, T. Fujiwara, A. Mizoguchi, and Y. Takai.
1217   2017. NGL-3-induced presynaptic differentiation of hippocampal neurons in an afadin-dependent, nectin-1-independent
1218   manner. *Genes Cells.* 22:742–755. doi:10.1111/gtc.12510.

1219 McDonough, S.I., K.J. Swartz, I.M. Mintz, L.M. Boland, and B.P. Bean. 1996. Inhibition of calcium channels in rat central and
1220   peripheral neurons by omega-conotoxin MVIIC. *J Neurosci.* 16:2612–2623. doi:10.1523/JNEUROSCI.16-08-02612.1996.

1221 Meaburn, K.J., E. Cabuy, G. Bonne, N. Levy, G.E. Morris, G. Novelli, I.R. Kill, and J.M. Bridger. 2007. Primary laminopathy
1222   fibroblasts display altered genome organization and apoptosis. *Aging Cell.* 6:139–153. doi:10.1111/j.1474-
1223   9726.2007.00270.x.

35

1224 Merideth, M.A., L.B. Gordon, S. Clauss, V. Sachdev, A.C.M. Smith, M.B. Perry, C.C. Brewer, C. Zalewski, H.J. Kim, B. Solomon,
1225 B.P. Brooks, L.H. Gerber, M.L. Turner, D.L. Domingo, T.C. Hart, J. Graf, J.C. Reynolds, A. Gropman, J.A. Yanovski, M.
1226 Gerhard-Herman, F.S. Collins, E.G. Nabel, R.O. Cannon, W.A. Gahl, and W.J. Introne. 2008. Phenotype and Course of
1227 Hutchinson–Gilford Progeria Syndrome. *N. Engl. J. Med.* 358:592–604. doi:10.1145/2503210.2503268.

1228 Metra, M., and J.R. Teerlink. 2017. Heart failure. *Lancet*. 390:1981–1995. doi:10.1016/S0140-6736(17)31071-1.

1229 Mewborn, S.K., M.J. Puckelwartz, F. Abuisneineh, J.P. Fahrenbach, Y. Zhang, H. MacLeod, L. Dellefave, P. Pytel, S. Selig,
1230 C.M. Labno, K. Reddy, H. Singh, and E. McNally. 2010. Altered chromosomal positioning, Compaction, and gene
1231 expression with a lamin A/C gene mutation. *PLoS One*. 5:e14342. doi:10.1371/journal.pone.0014342.

1232 Molkentin, J.D., J.R. Lu, C.L. Antos, B. Markham, J. Richardson, J. Robbins, S.R. Grant, and E.N. Olson. 1998. A calcineurin-
1233 dependent transcriptional pathway for cardiac hypertrophy. *Cell*. 93:215–28. doi:10.1016/S0092-8674(00)81573-1.

1234 Mosqueira, D., I. Mannhardt, J.R. Bhagwan, K. Lis-Slimak, P. Katili, E. Scott, M. Hassan, M. Prondzynski, S.C. Harmer, A.
1235 Tinker, J.G.W. Smith, L. Carrier, P.M. Williams, D. Gaffney, T. Eschenhagen, A. Hansen, and C. Denning. 2018.
1236 CRISPR/Cas9 editing in human pluripotent stem cell-cardiomyocytes highlights arrhythmias, hypocontractility, and energy
1237 depletion as potential therapeutic targets for hypertrophic cardiomyopathy. *Eur. Heart J.* 39:3879–3892.
1238 doi:10.1093/eurheartj/ehy249.

1239 Muchir, A., P. Pavlidis, V. Decostre, A.J. Herron, T. Arimura, G. Bonne, and H.J. Worman. 2007. Activation of MAPK pathways
1240 links LMNA mutations to cardiomyopathy in Emery-Dreifuss muscular dystrophy. *J. Clin. Invest.* 117:1282–93.
1241 doi:10.1172/JCI29042.

1242 Muchir, A., W. Wu, J.C. Choi, S. Iwata, J. Morrow, S. Homma, and H.J. Worman. 2012. Abnormal p38 mitogen-activated protein
1243 kinase signaling in dilated cardiomyopathy caused by lamin A/C gene mutation. *Hum. Mol. Genet.* 21:4325–4333.
1244 doi:10.1093/hmg/dds265.

1245 Nakamura, T.Y., Y. Iwata, Y. Arai, K. Komamura, and S. Wakabayashi. 2008. Activation of Na+/H+ Exchanger 1 Is Sufficient to
1246 Generate Ca2+ Signals That Induce Cardiac Hypertrophy and Heart Failure. *Circ. Res.* 103:891–899.
1247 doi:10.1161/CIRCRESAHA.108.175141.

1248 Nie, J., Q. Duan, M. He, X. Li, B. Wang, C. Zhou, L. Wu, Z. Wen, C. Chen, D.W. Wang, K.M. Alsina, X.H.T. Wehrens, D.W.
1249 Wang, and L. Ni. 2018. Ranolazine prevents pressure overload-induced cardiac hypertrophy and heart failure by restoring
1250 aberrant Na+ and Ca2+ handling. *J. Cell. Physiol.* doi:10.1002/jcp.27791.

1251 Nimmrich, V., and G. Gross. 2012. P/Q-type calcium channel modulators. *Br. J. Pharmacol.* 167:741–759. doi:10.1111/j.1476-
1252 5381.2012.02069.x.

1253 Nora, E.P., B.R. Lajoie, E.G. Schulz, L. Giorgetti, I. Okamoto, N. Servant, T. Piolot, N.L. van Berkum, J. Meisig, J. Sedat, J.
1254 Gribnau, E. Barillot, N. Blüthgen, J. Dekker, and E. Heard. 2012. Spatial partitioning of the regulatory landscape of the X-
1255 inactivation centre. *Nature*. 485:381–385. doi:10.1038/nature11049.

1256 Ortmann, D., and L. Vallier. 2017. Variability of human pluripotent stem cell lines. *Curr. Opin. Genet. Dev.* 46:179–185.
1257 doi:10.1016/j.gde.2017.07.004.

1258 Pan, H., A.A. Richards, X. Zhu, J.A. Joglar, H.L. Yin, and V. Garg. 2009. A novel mutation in LAMIN A/C is associated with
1259 isolated early-onset atrial fibrillation and progressive atrioventricular block followed by cardiomyopathy and sudden cardiac
1260 death. *Hear. Rhythm*. 6:707–710. doi:10.1016/j.hrthm.2009.01.037.

1261 Peroz, D., N. Rodriguez, F. Choveau, I. Baró, J. Mérot, and G. Loussouarn. 2008. Kv7.1 (KCNQ1) properties and
1262 channelopathies. *J. Physiol.* 586:1785–1789. doi:10.1113/jphysiol.2007.148254.

1263 Rajakulendran, S., D. Kaski, and M.G. Hanna. 2012. Neuronal P/Q-type calcium channel dysfunction in inherited disorders of
1264 the CNS. *Nat. Rev. Neurol.* 8:86–96. doi:10.1038/nrneurol.2011.228.

1265 Ramani, V., D.A. Cusanovich, R.J. Hause, W. Ma, R. Qiu, X. Deng, C.A. Blau, C.M. Disteche, W.S. Noble, J. Shendure, and Z.
1266 Duan. 2016. Mapping 3D genome architecture through in situ DNase Hi-C. *Nat Protoc*. 11:2104–2121.
1267 doi:10.1038/nprot.2016.126.

1268 Ramos, F.J., S.C. Chen, M.G. Garelick, D.-F. Dai, C.-Y. Liao, K.H. Schreiber, V.L. MacKay, E.H. An, R. Strong, W.C. Ladiges,
1269 P.S. Rabinovitch, M. Kaeberlein, and B.K. Kennedy. 2012. Rapamycin reverses elevated mTORC1 signaling in lamin A/C-
1270 deficient mice, rescues cardiac and skeletal muscle function, and extends survival. *Sci. Transl. Med.* 4:144ra103.
1271 doi:10.1126/scitranslmed.3003802.

1272 Ran, F.A., P.D. Hsu, J. Wright, V. Agarwala, D.A. Scott, and F. Zhang. 2013. Genome engineering using the CRISPR-Cas9
1273 system. *Nat. Protoc.* 8:2281–308. doi:10.1038/nprot.2013.143.

1274 Rao, S.S.P., M.H. Huntley, N.C. Durand, E.K. Stamenova, I.D. Bochkov, J.T. Robinson, A.L. Sanborn, I. Machol, A.D. Omer,
1275 E.S. Lander, and E.L. Aiden. 2014. A 3D map of the human genome at kilobase resolution reveals principles of chromatin
1276 looping. *Cell*. 159:1665–1680. doi:10.1016/j.cell.2014.11.021.

1277 Rast, G., U. Kraushaar, S. Buckenmaier, C. Ittrich, and B.D. Guth. 2016. Influence of field potential duration on spontaneous

beating rate of human induced pluripotent stem cell-derived cardiomyocytes: Implications for data analysis and test system selection. *J. Pharmacol. Toxicol. Methods*. 82:74–82. doi:10.1016/j.vascn.2016.08.002.

Redin, C., H. Brand, R.L. Collins, T. Kammin, E. Mitchell, J.C. Hodge, C. Hanscom, V. Pillalamarri, C.M. Seabra, M.-A. Abbott, O.A. Abdul-Rahman, E. Aberg, R. Adley, S.L. Alcaraz-Estrada, F.S. Alkuraya, Y. An, M.-A. Anderson, C. Antolik, K. Anyane-Yeboa, J.F. Atkin, T. Bartell, J.A. Bernstein, E. Beyer, I. Blumenthal, E.M.H.F. Bongers, E.H. Brilstra, C.W. Brown, H.T. Brüggenwirth, B. Callewaert, C. Chiang, K. Corning, H. Cox, E. Cuppen, B.B. Currall, T. Cushing, D. David, M.A. Deardorff, A. Dheedene, M. D'Hooghe, B.B.A. de Vries, D.L. Earl, H.L. Ferguson, H. Fisher, D.R. FitzPatrick, P. Gerrol, D. Giachino, J.T. Glessner, T. Gliem, M. Grady, B.H. Graham, C. Griffis, K.W. Gripp, A.L. Gropman, A. Hanson-Kahn, D.J. Harris, M.A. Hayden, R. Hill, R. Hochstenbach, J.D. Hoffman, R.J. Hopkin, M.W. Hubshman, A.M. Innes, M. Irons, M. Irving, J.C. Jacobsen, S. Janssens, T. Jewett, J.P. Johnson, M.C. Jongmans, S.G. Kahler, D.A. Koolen, J. Korzelius, P.M. Kroisel, Y. Lacassie, W. Lawless, E. Lemyre, K. Leppig, A. V Levin, H. Li, H. Li, E.C. Liao, C. Lim, E.J. Lose, D. Lucente, M.J. Macera, P. Manavalan, G. Mandrile, C.L. Marcelis, L. Margolin, T. Mason, D. Masser-Frye, M.W. McClellan, C.J.Z. Mendoza, B. Menten, S. Middelkamp, L.R. Mikami, E. Moe, S. Mohammed, et al. 2017. The genomic landscape of balanced cytogenetic abnormalities associated with human congenital anomalies. *Nat. Genet.* 49:36–45. doi:10.1038/ng.3720.

Van Rijsingen, I.A.W., E. Arbustini, P.M. Elliott, J. Mogensen, J.F. Hermans-Van Ast, A.J. Van Der Kooi, J.P. Van Tintelen, M.P. Van Den Berg, A. Pilotto, M. Pasotti, S. Jenkins, C. Rowland, U. Aslam, A.A.M. Wilde, A. Perrot, S. Pankuweit, A.H. Zwinderman, P. Charron, and Y.M. Pinto. 2012. Risk factors for malignant ventricular arrhythmias in Lamin A/C mutation carriers: A European cohort study. *J. Am. Coll. Cardiol.* 59:493–500. doi:10.1016/j.jacc.2011.08.078.

Roncarati, R., C. Viviani Anselmi, P. Krawitz, G. Lattanzi, Y. von Kodolitsch, A. Perrot, E. di Pasquale, L. Papa, P. Portararo, M. Columbaro, A. Forni, G. Faggian, G. Condorelli, and P.N. Robinson. 2013. Doubly heterozygous LMNA and TTN mutations revealed by exome sequencing in a severe form of dilated cardiomyopathy. *Eur. J. Hum. Genet.* 21:1105–11. doi:10.1038/ejhg.2013.16.

Ruan, J.L., N.L. Tulloch, M. V Razumova, M. Saiget, V. Muskheli, L. Pabon, H. Reinecke, M. Regnier, and C.E. Murry. 2016. Mechanical Stress Conditioning and Electrical Stimulation Promote Contractility and Force Maturation of Induced Pluripotent Stem Cell-Derived Human Cardiac Tissue. *Circulation*. 134:1557–1567. doi:10.1161/CIRCULATIONAHA.114.014998.

Russo, V., A. Rago, L. Politano, A.A. Papa, F. Di Meo, M.G. Russo, P. Golino, R. Calabrò, and G. Nigro. 2012. Increased dispersion of ventricular repolarization in emery dreifuss muscular dystrophy patients. *Med Sci Monit*. 18:643–647. doi:10.12659/MSM.883541.

Saga, A., A. Karibe, J. Otomo, K. Iwabuchi, T. Takahashi, H. Kanno, J. Kikuchi, M. Keitoku, T. Shinozaki, and H. Shimokawa. 2009. Lamin A/C gene mutations in familial cardiomyopathy with advanced atrioventricular block and arrhythmia. *Tohoku J. Exp. Med.* 218:309–16. doi:doi.org/10.1620/tjem.218.309.

Sala, L., M. Bellin, and C.L. Mummery. 2017. Integrating cardiomyocytes from human pluripotent stem cells in safety pharmacology: has the time come? *Br. J. Pharmacol.* 174:3749–3765. doi:10.1111/bph.13577.

Schmitt, A.D., M. Hu, I. Jung, Z. Xu, Y. Qiu, C.L. Tan, Y. Li, S. Lin, Y. Lin, C.L. Barr, and B. Ren. 2016. A Compendium of Chromatin Contact Maps Reveals Spatially Active Regions in the Human Genome. *Cell Rep.* 17:2042–2059. doi:10.1016/j.celrep.2016.10.061.

Servant, N., N. Varoquaux, B.R. Lajoie, E. Viara, C.-J. Chen, J.-P. Vert, E. Heard, J. Dekker, and E. Barillot. 2015. HiC-Pro: an optimized and flexible pipeline for Hi-C data processing. *Genome Biol.* 16:259. doi:10.1186/s13059-015-0831-x.

Sexton, T., E. Yaffe, E. Kenigsberg, F. Bantignies, B. Leblanc, M. Hoichman, H. Parrinello, A. Tanay, and G. Cavalli. 2012. Three-Dimensional Folding and Functional Organization Principles of the Drosophila Genome. *Cell*. 148:458–472. doi:10.1016/j.cell.2012.01.010.

Simonis, M., P. Klous, E. Splinter, Y. Moshkin, R. Willemsen, E. de Wit, B. van Steensel, and W. de Laat. 2006. Nuclear organization of active and inactive chromatin domains uncovered by chromosome conformation capture–on-chip (4C). *Nat. Genet.* 38:1348–1354. doi:10.1038/ng1896.

Siu, C.W., Y.K. Lee, J.C.Y. Ho, W.H. Lai, Y.C. Chan, K.M. Ng, L.Y. Wong, K.W. Au, Y.M. Lau, J. Zhang, K.W. Lay, A. Colman, and H.F. Tse. 2012. Modeling of lamin A/C mutation premature cardiac aging using patient-specific induced pluripotent stem cells. *Aging*. 4:803–822. doi:10.18632/aging.100503.

Slaymaker, I.M., L. Gao, B. Zetsche, D. a. Scott, W.X. Yan, and F. Zhang. 2015. Rationally engineered Cas9 nucleases with improved specificity. *Science*. 351:84–88. doi:10.1126/science.aad5227.

Sniadecki, N.J., and C.S. Chen. 2007. Microfabricated Silicone Elastomeric Post Arrays for Measuring Traction Forces of Adherent Cells. *In* Methods in Cell Biology. 313–328.

Solovei, I., A.S. Wang, K. Thanisch, C.S. Schmidt, S. Krebs, M. Zwerger, T. V Cohen, D. Devys, R. Foisner, L. Peichl, H.

Herrmann, H. Blum, D. Engelkamp, C.L. Stewart, H. Leonhardt, and B. Joffe. 2013. LBR and lamin A/C sequentially tether peripheral heterochromatin and inversely regulate differentiation. *Cell*. 152:584–598. doi:10.1016/j.cell.2013.01.009.

van Steensel, B., and A.S. Belmont. 2017. Lamina-Associated Domains: Links with Chromosome Architecture, Heterochromatin, and Gene Repression. *Cell*. 169:780–791. doi:10.1016/j.cell.2017.04.022.

Stevens, T.J., D. Lando, S. Basu, L.P. Atkinson, Y. Cao, S.F. Lee, M. Leeb, K.J. Wohlfahrt, W. Boucher, A. O'Shaughnessy-Kirwan, J. Cramard, A.J. Faure, M. Ralser, E. Blanco, L. Morey, M. Sansó, M.G.S. Palayret, B. Lehner, L. Di Croce, A. Wutz, B. Hendrich, D. Klenerman, and E.D. Laue. 2017. 3D structures of individual mammalian genomes studied by single-cell Hi-C. *Nature*. 544:59–64. doi:10.1038/nature21429.

Strate, I., F. Tessadori, and J. Bakkers. 2015. Glypican4 promotes cardiac specification and differentiation by attenuating canonical Wnt and Bmp signaling. *Development*. 142:1767–1776. doi:10.1242/dev.113894.

Sun, J.H., L. Zhou, D.J. Emerson, S.A. Phyo, K.R. Titus, W. Gong, T.G. Gilgenast, J.A. Beagan, B.L. Davidson, F. Tassone, and J.E. Phillips-Cremins. 2018. Disease-Associated Short Tandem Repeats Co-localize with Chromatin Domain Boundaries. *Cell*. 175:224–238.e15. doi:10.1016/j.cell.2018.08.005.

Taniura, H., C. Glass, and L. Gerace. 1995. A chromatin binding site in the tail domain of nuclear lamins that interacts with core histones. *J. Cell Biol.* 131:33–44. doi:10.1083/jcb.131.1.33.

Thorvaldsdóttir, H., J.T. Robinson, and J.P. Mesirov. 2013. Integrative Genomics Viewer (IGV): high-performance genomics data visualization and exploration. *Brief. Bioinform.* 14:178–92. doi:10.1093/bib/bbs017.

van Tintelen, J.P., R.M.W. Hofstra, H. Katerberg, T. Rossenbacker, A.C.P. Wiesfeld, G.J. du Marchie Sarvaas, A.A.M. Wilde, I.M. van Langen, E.A. Nannenberg, A.J. van der Kooi, M. Kraak, I.C. van Gelder, D.J. van Veldhuisen, Y. Vos, and M.P. van den Berg. 2007a. High yield of LMNA mutations in patients with dilated cardiomyopathy and/or conduction disease referred to cardiogenetics outpatient clinics. *Am. Heart J.* 154:1130–9. doi:10.1016/j.ahj.2007.07.038.

van Tintelen, J.P., R.A. Tio, W.S. Kerstjens-Frederikse, J.H. van Berlo, L.G. Boven, A.J.H. Suurmeijer, S.J. White, J.T. den Dunnen, G.J. te Meerman, Y.J. Vos, A.H. van der Hout, J. Osinga, M.P. van den Berg, D.J. van Veldhuisen, C.H.C.M. Buys, R.M.W. Hofstra, and Y.M. Pinto. 2007b. Severe myocardial fibrosis caused by a deletion of the 5' end of the lamin A/C gene. *J. Am. Coll. Cardiol.* 49:2430–9. doi:10.1016/j.jacc.2007.02.063.

Tobita, T., S. Nomura, T. Fujita, Y. Morita, Y. Asano, K. Onoue, M. Ito, Y. Imai, A. Suzuki, T. Ko, M. Satoh, K. Fujita, A.T. Naito, Y. Furutani, H. Toko, M. Harada, E. Amiya, M. Hatano, E. Takimoto, T. Shiga, T. Nakanishi, Y. Sakata, M. Ono, Y. Saito, S. Takashima, N. Hagiwara, H. Aburatani, and I. Komuro. 2018. Genetic basis of cardiomyopathy and the genotypes involved in prognosis and left ventricular reverse remodeling. *Sci. Rep.* 8:1–11. doi:10.1038/s41598-018-20114-9.

Trapnell, C., A. Roberts, L. Goff, G. Pertea, D. Kim, D.R. Kelley, H. Pimentel, S.L. Salzberg, J.L. Rinn, and L. Pachter. 2012. Differential gene and transcript expression analysis of RNA-seq experiments with TopHat and Cufflinks. *Nat. Protoc.* 7:562–578. doi:10.1038/nprot.2012.016.

Trapnell, C., B.A. Williams, G. Pertea, A. Mortazavi, G. Kwan, M.J. van Baren, S.L. Salzberg, B.J. Wold, and L. Pachter. 2010. Transcript assembly and quantification by RNA-Seq reveals unannotated transcripts and isoform switching during cell differentiation. *Nat. Biotechnol.* 28:511–515. doi:10.1038/nbt.1621.

Vandael, E., B. Vandenberk, J. Vandenberghe, R. Willems, and V. Foulon. 2017. Risk factors for QTc-prolongation: systematic review of the evidence. *Int. J. Clin. Pharm.* 39:16–25. doi:10.1007/s11096-016-0414-2.

Wang, Y., A. Khan, S. Heringer-Walther, H.-P. Schultheiss, M. da C. V Moreira, and T. Walther. 2013. Prognostic value of circulating levels of stem cell growth factor beta (SCGF beta) in patients with Chagas' disease and idiopathic dilated cardiomyopathy. *Cytokine*. 61:728–31. doi:10.1016/j.cyto.2012.12.018.

Won, H., L. de la Torre-Ubieta, J.L. Stein, N.N. Parikshak, J. Huang, C.K. Opland, M.J. Gandal, G.J. Sutton, F. Hormozdiari, D. Lu, C. Lee, E. Eskin, I. Voineagu, J. Ernst, and D.H. Geschwind. 2016. Chromosome conformation elucidates regulatory relationships in developing human brain. *Nature*. 538:523–27. doi:10.1038/nature19847.

Worman, H.J., and J.-C. Courvalin. 2004. How do mutations in lamins A and C cause disease? *J. Clin. Invest.* 113:349–51. doi:10.1172/JCI20832.

Yang, T., F. Zhang, G.G. Yardımcı, F. Song, R.C. Hardison, W.S. Noble, F. Yue, and Q. Li. 2017. HiCRep: assessing the reproducibility of Hi-C data using a stratum-adjusted correlation coefficient. *Genome Res.* 27:1939–1949. doi:10.1101/gr.220640.117.

Yang, X., L. Pabon, and C.E. Murry. 2014. Engineering adolescence: Maturation of human pluripotent stem cell-derived cardiomyocytes. *Circ. Res.* 114:511–523. doi:10.1161/CIRCRESAHA.114.300558.

Ye, Q., and H.J. Worman. 1994. Primary structure analysis and lamin B and DNA binding of human LBR, an integral protein of the nuclear envelope inner membrane. *J. Biol. Chem.* 269:11306–11.

Ye, Q., and H.J. Worman. 1996. Interaction between an integral protein of the nuclear envelope inner membrane and human chromodomain proteins homologous to Drosophila HP1. *J. Biol. Chem.* 271:14653–6. doi:10.1074/jbc.271.25.14653.

Yu, M., and B. Ren. 2017. The Three-Dimensional Organization of Mammalian Genomes. *Annu. Rev. Cell Dev. Biol.* 33:265–289. doi:10.1146/annurev-cellbio-100616-060531.

Yuan, J., G. Simos, G. Blobel, and S.D. Georgatos. 1991. Binding of lamin A to polynucleosomes. *J. Biol. Chem.* 266:9211–5.

Yusa, K. 2013. Seamless genome editing in human pluripotent stem cells using custom endonuclease-based gene targeting and the piggyBac transposon. *Nat. Protoc.* 8:2061–78. doi:10.1038/nprot.2013.126.

Yusa, K., S.T. Rashid, H. Strick-Marchand, I. Varela, P.-Q. Liu, D.E. Paschon, E. Miranda, A. Ordóñez, N.R.F. Hannan, F.J. Rouhani, S. Darche, G. Alexander, S.J. Marciniak, N. Fusaki, M. Hasegawa, M.C. Holmes, J.P. Di Santo, D. a Lomas, A. Bradley, and L. Vallier. 2011. Targeted gene correction of α1-antitrypsin deficiency in induced pluripotent stem cells. *Nature.* 478:391–4. doi:10.1038/nature10424.

Zhang, X., X. Ai, H. Nakayama, B. Chen, D.M. Harris, M. Tang, Y. Xie, C. Szeto, Y. Li, Y. Li, H. Zhang, A.D. Eckhart, W.J. Koch, J.D. Molkentin, and X. Chen. 2016. Persistent increases in Ca2+ influx through Cav1.2 shortens action potential and causes Ca2+ overload-induced afterdepolarizations and arrhythmias. *Basic Res. Cardiol.* 111. doi:10.1007/s00395-015-0523-4.

Zheng, X., J. Hu, S. Yue, L. Kristiani, M. Kim, M. Sauria, J. Taylor, Y. Kim, and Y. Zheng. 2018. Lamins Organize the Global Three-Dimensional Genome from the Nuclear Periphery. *Mol. Cell.* 71:802–815.e7. doi:10.1016/j.molcel.2018.05.017.

Zheng, X., Y. Kim, and Y. Zheng. 2015. Identification of lamin B-regulated chromatin regions based on chromatin landscapes. *Mol. Biol. Cell.* 26:2685–2697. doi:10.1091/mbc.E15-04-0210.

Abbreviations

3D-EHT(s): three-dimensional engineered heart tissue(s)

A/B: active/inactive (chromatin compartment)

CCQ: contraction correlation quantification

FPD: field potential duration

DCM: dilated cardiomyopathy

Hi-C: genome-wide chromosome conformation capture

hESC(s): human embryonic stem cell(s)

hESC-CM(s): human embryonic stem cell-derived cardiomyocyte(s)

hiPSC(s): human induced pluripotent stem cell(s)

hiPSC-CM(s): human induced pluripotent stem cell-derived cardiomyocyte(s)

LAD(s): lamin-associated domains

MEA(s): multi-electrode array(s)

PC: principal component

RNA-seq: ribonucleic acid sequencing

RT-qPCR: quantitative reverse transcription polymerase chain reaction

TAD(s): topologically associating domain(s)

Figures and figure legends

1422
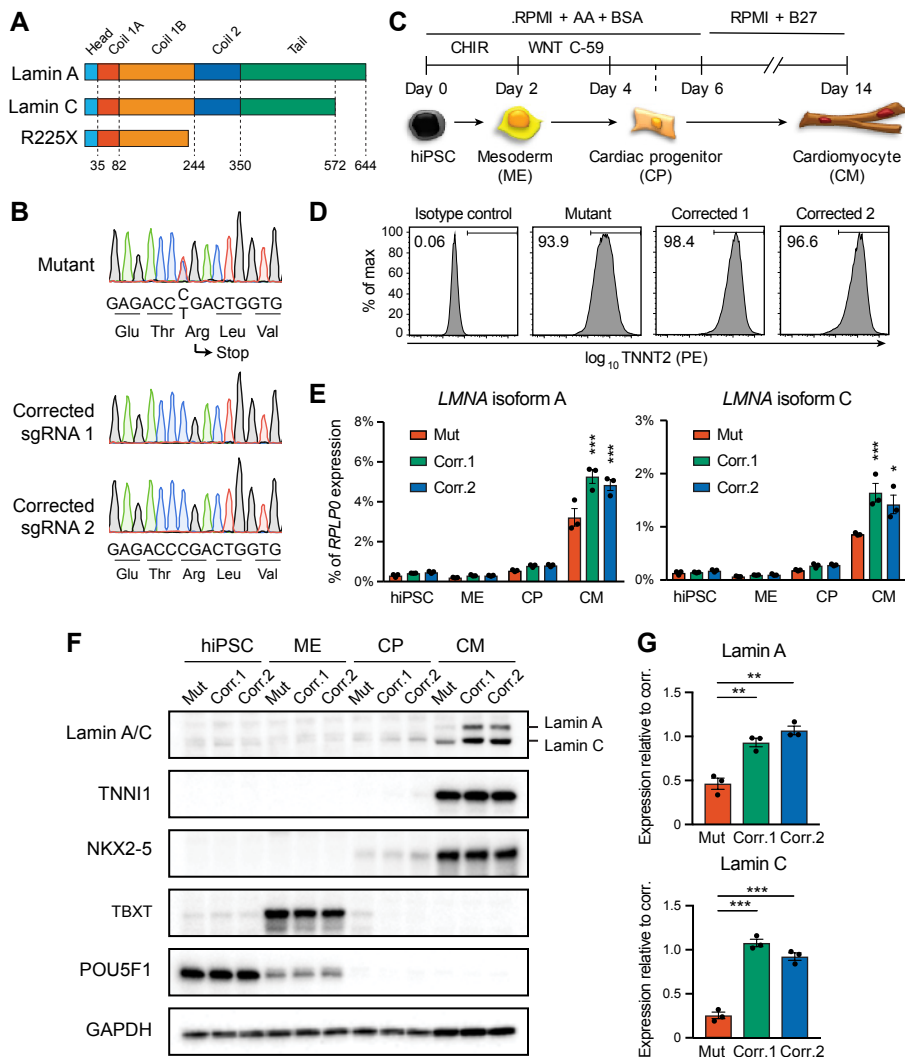
Figure 1. Generation of lamin A/C haploinsufficient hiPSC-CMs.

(**A**) Predicted effect of the *LMNA* R225X mutation on the two splicing products lamin A and C. Key protein domains and their location along the amino acid sequence are indicated. (**B**) Sanger sequencing of *LMNA* exon 4 in hiPSCs with heterozygous R225X mutation (top), or in hiPSCs obtained after CRISPR/Cas9-based scarless correction of the mutation (bottom). (**C**) Schematic of the protocol for step-wise directed differentiation of hiPSC-CMs. CHIR: CHIR99021 (WNT activator); WNT C-59: WNT inhibitor; AA: ascorbic acid. (**D**) Quantification of cardiac differentiation efficiency by flow cytometry for cardiac troponin T (TNNT2) on hiPSC-CMs at day 14 of differentiation. The percentage of TNNT2+ cells is reported. (**E**) RT-qPCR analyses at the indicated stages of hiPSC-CM differentiation (see panel C). Differences *versus* mutant were calculated by two-way ANOVA with post-hoc Holm-Sidak binary comparisons (* = $p < 0.05$, *** = $p < 0.001$; n = 3 differentiations; average ± SEM). (**F**) Representative western blot for lamin A/C and differentiation markers during iPSC-CM differentiation. (**G**) Quantification of lamin A/C expression in hiPSC-CMs from western blot densitometries (n = 3 differentiations; average ± SEM). Differences
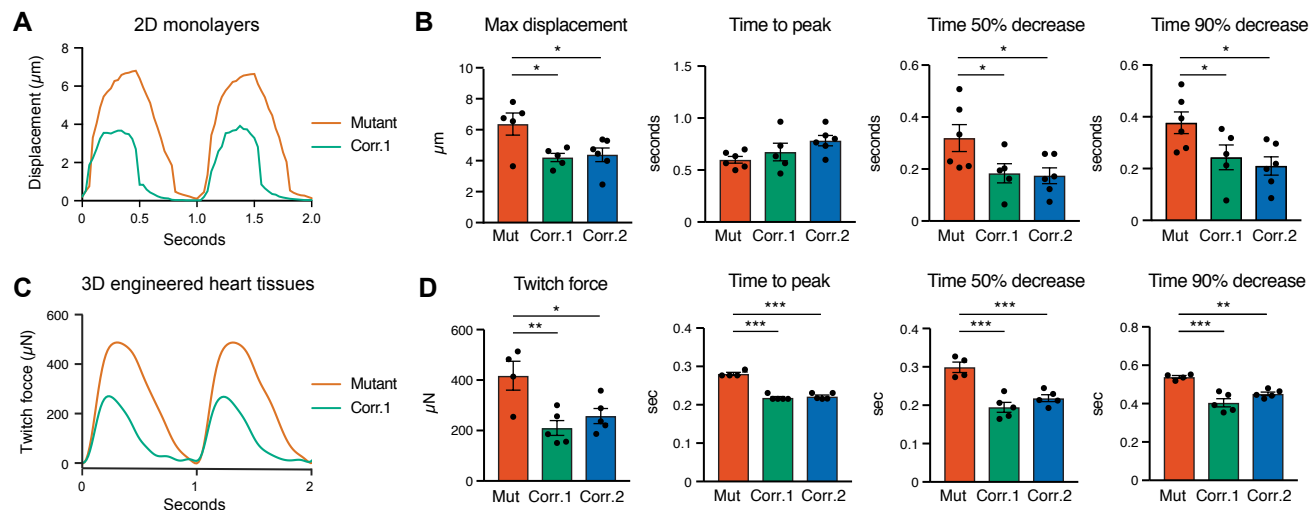
1435   versus mutant were calculated by one-way ANOVA with post-hoc Holm-Sidak binary comparisons (** = $p < 0.01$,

1436   *** = $p < 0.001$; n = 3 differentiations; average ± SEM). Throughout the figure (and in all other figures), Mut or Mutant

1437   indicates *LMNA* R225X hiPSCs, and Corr.1/2 or Corrected 1/2 indicate the two isogenic corrected control *LMNA*

1438   R225R hiPSC lines.

1439
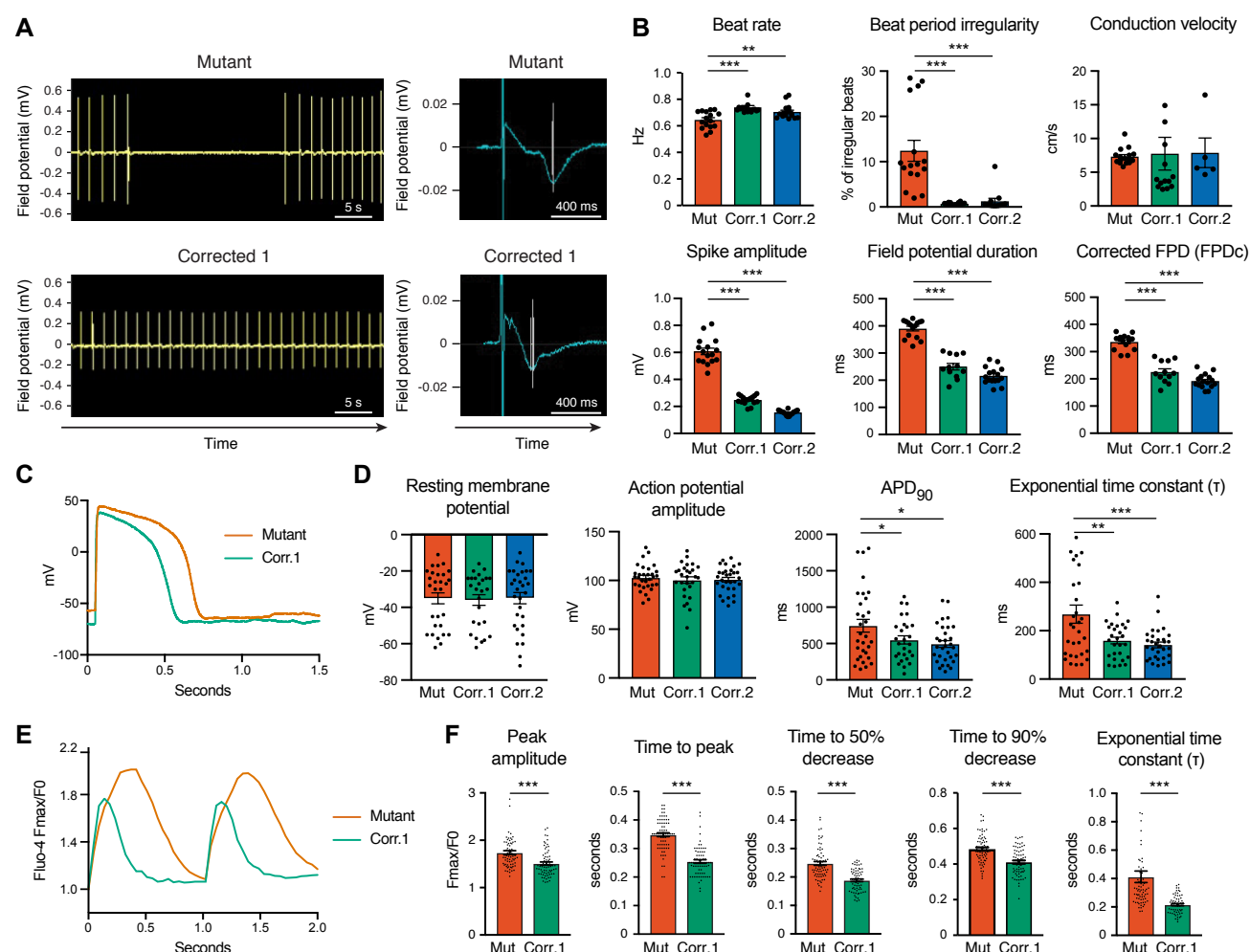
**Figure 2. Electrophysiological properties of lamin A/C haploinsufficient hiPSC-CMs.**

(**A**) Representative traces from MEA recordings of spontaneous electrical activity in hiPSC-CM monolayers. On the right, the average field potential changes during an individual beat are reported, and depolarization and repolarization timings are indicated by vertical lines. (**B**) Representative quantifications of electrophysiological properties from MEA analyses. Differences *versus* mutant were calculated by one-way ANOVA with post-hoc Holm-Sidak binary comparisons (** = $p < 0.01$, *** = $p < 0.001$; n = 5-16 wells; average ± SEM). (**C**) Representative voltage recordings by whole-cell patch clamp during evoked action potentials in individual hiPSC-CMs. (**D**) Quantifications of electrophysiological properties from whole-cell patch clamp analyses. Differences *versus* mutant were calculated by one-way ANOVA with post-hoc Holm-Sidak binary comparisons (* = $p < 0.05$, ** = $p < 0.01$, *** = $p < 0.001$; n = 26-30 cells from two differentiations; average ± SEM). (**E**) Representative optical recordings of calcium fluxes with Fluo-4 in hiPSC-CM monolayers electrically paced at 1 Hz. (**F**) Representative quantifications of calcium fluxes properties. Differences *versus* mutant were calculated by unpaired t-test (*** = $p < 0.001$; n = 69-70 cells; average ± SEM).

Figure 3. Contractile properties of lamin A/C haploinsufficient hiPSC-CMs.

(**A**) Representative measurements of cellular displacement during contraction of hiPSC-CM monolayers electrically paced at 1 Hz. (**B**) Representative quantifications of cell contractility from analyses of optical recordings. Differences *versus* mutant were calculated by one-way ANOVA with post-hoc Holm-Sidak binary comparisons (* = $p < 0.05$; n = 5-6 field of views; average ± SEM). (**C**) Representative measurements of twitch force during contraction of 3D-EHTs electrically paced at 1 Hz. (**D**) Representative quantifications of tissue contractility from analyses of optical recordings. Differences *versus* mutant were calculated by one-way ANOVA with post-hoc Holm-Sidak binary comparisons (* = $p < 0.05$, ** = $p < 0.01$, *** = $p < 0.001$; n = 4-5 3D-EHTs; average ± SEM).

1462
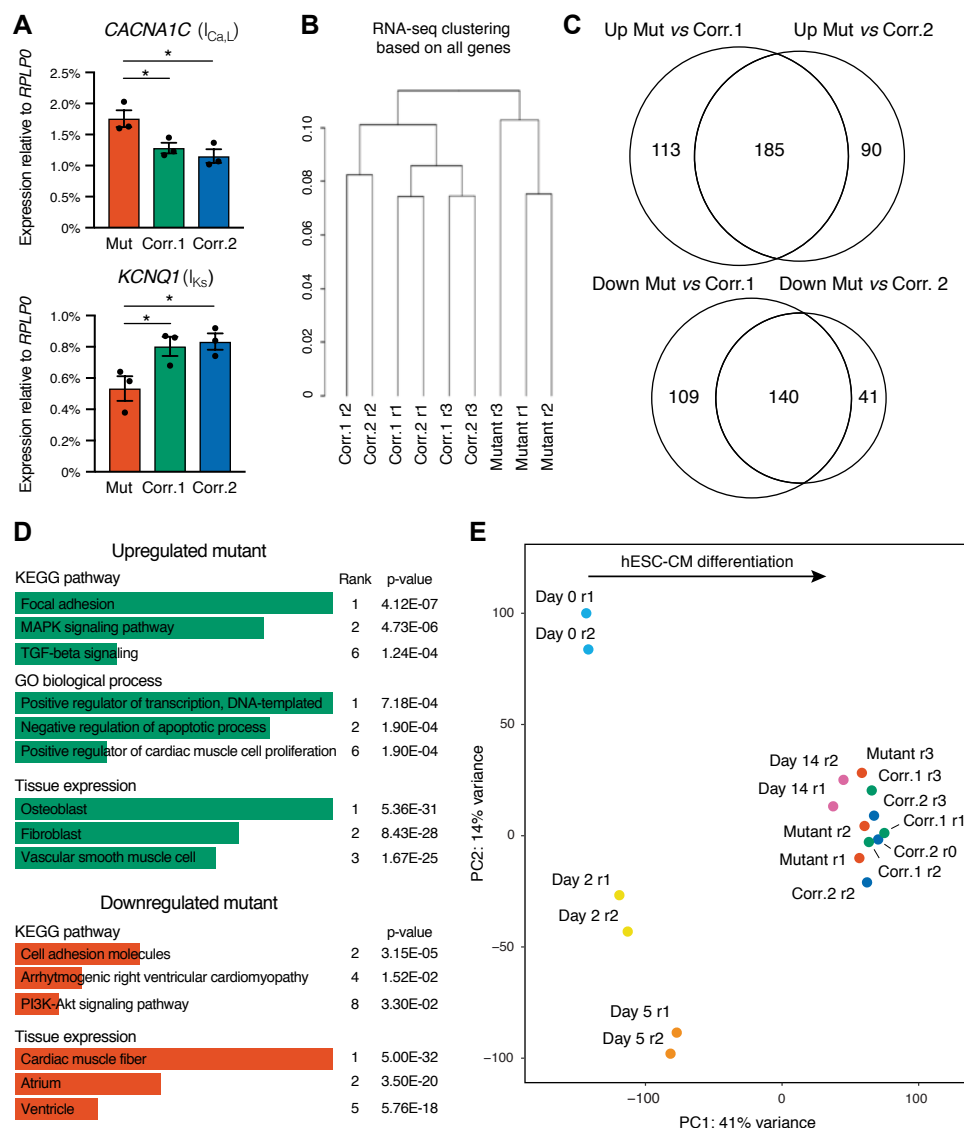
1463 **Figure 4. Gene expression changes in lamin A/C haploinsufficient hiPSC-CMs.**

1464 (**A**) RT-qPCR analyses in hiPSC-CMs at day 14 of differentiation. Differences *versus* mutant were calculated by

1465 one-way ANOVA with post-hoc Holm-Sidak binary comparisons (* = $p < 0.05$, n = 3 differentiations; average ±

1466 SEM). (**B**) Hierarchical clustering of hiPSC-CMs analyzed by RNA-seq based on all expressed genes. Biological

1467 replicates from 3 independent differentiations were analyzed (r1, r2, r3). (**C**) Overlap in genes up- or downregulated

1468 in mutant hiPSC-CMs *versus* hiPSC-CMs from the two corrected control lines (fold-change > 2 and q-value < 0.05;

1469 Table S1). (**D**) Selected results from ontology and pathway enrichment analyses of genes consistently up- or

1470 downregulation in mutant hiPSC-CMs. For each term, the rank and the corresponding p-value are reported (terms

1471 ranked by combined score; Table S2). (**E**) Linear dimensionality reduction by principal component analysis of RNA-

1472 seq data of mutant and corrected hiPSC-CMs, and hESC-CMs sampled at different time points of differentiation

1473 (Fields et al., 2017). The amount of variance captured by each of the two main principal components (PC) is

1474 reported, and the biological interpretation for the PC1 axis is indicated.

44
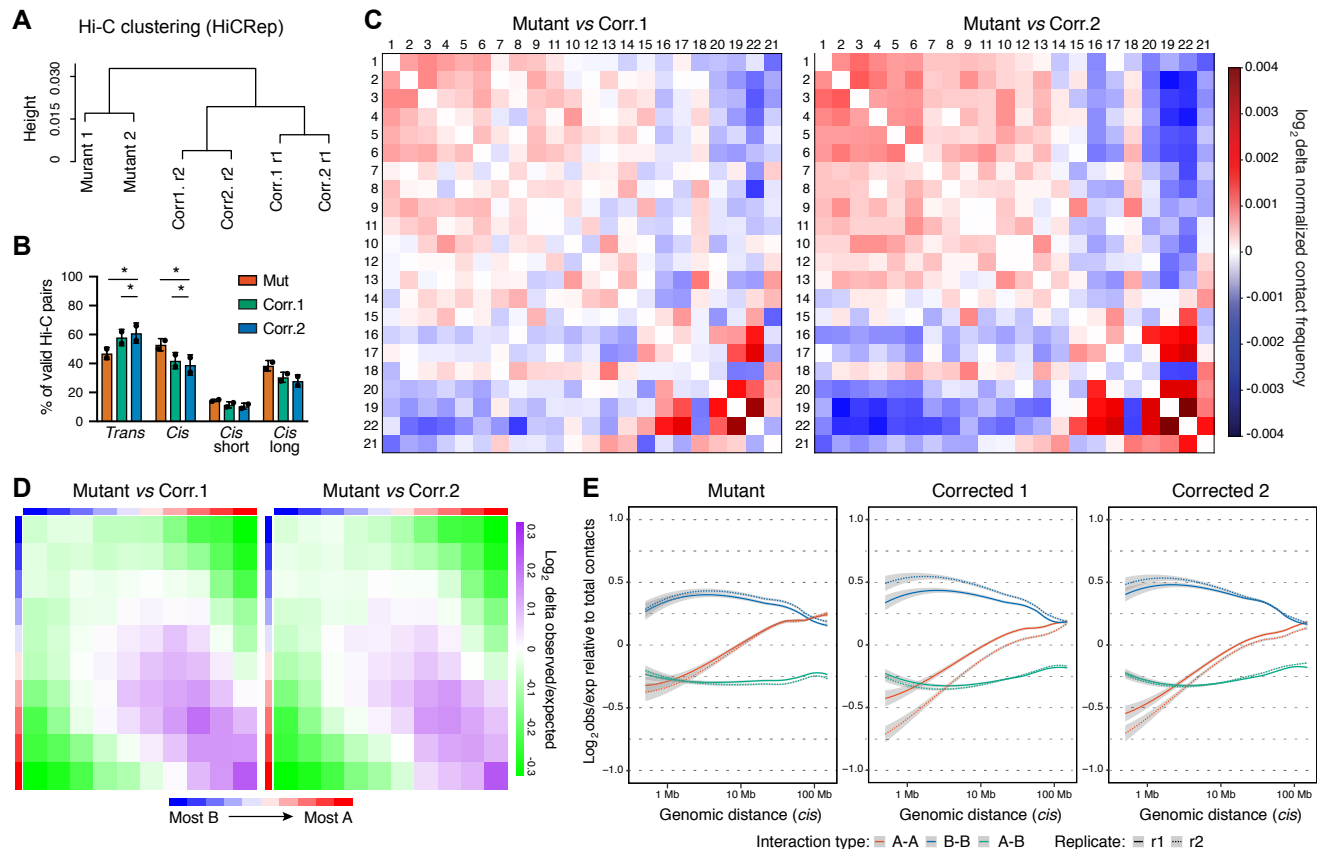
**Figure 5. Global properties of chromatin topology in lamin A/C haploinsufficient hiPSC-CMs.**

(**A**) Hierarchical clustering of hiPSC-CMs analyzed by *in situ* DNase Hi-C based on similarity scores between the genomic contact matrices calculated with HiCRep. Biological replicates from 2 independent differentiations were analyzed (r1, r2). (**B**) Proportion of genomic interactions between different chromosomes (*trans*) or within the same chromosome (*cis*) involving distances < 20 Kb (*cis* short) or > 20 Kb (*cis* long; Table S3). Differences *versus* mutant were calculated by two-way ANOVA with post-hoc Holm-Sidak binary comparisons (* = p < 0.05; n = 2 differentiations; average ± SEM). (**C**) Representative heatmaps of differential contact matrices between chromosomes. Autosomes are ranked based on their size from left to right and top to bottom. (**D**) Representative heatmaps of differential *cis* interactions between active (A) and inactive (B) chromatin compartments. 500 Kb genomic bins were assigned to ten deciles based on their PC1 score from the linear dimensionality reduction of the Hi-C matrix (from most B to most A; Table S4), and average observed/expected distance normalized scores for each pair of deciles were calculated. (**E**) Probability of *cis* genomic contacts over increasing genomic distance for regions in homotypic (A-A or B-B) or heterotypic (A-B) chromatin compartments. Values are normalized to all contacts observed at a given distance, and LOESS curves are shown (gray background: 95% confidence bands).
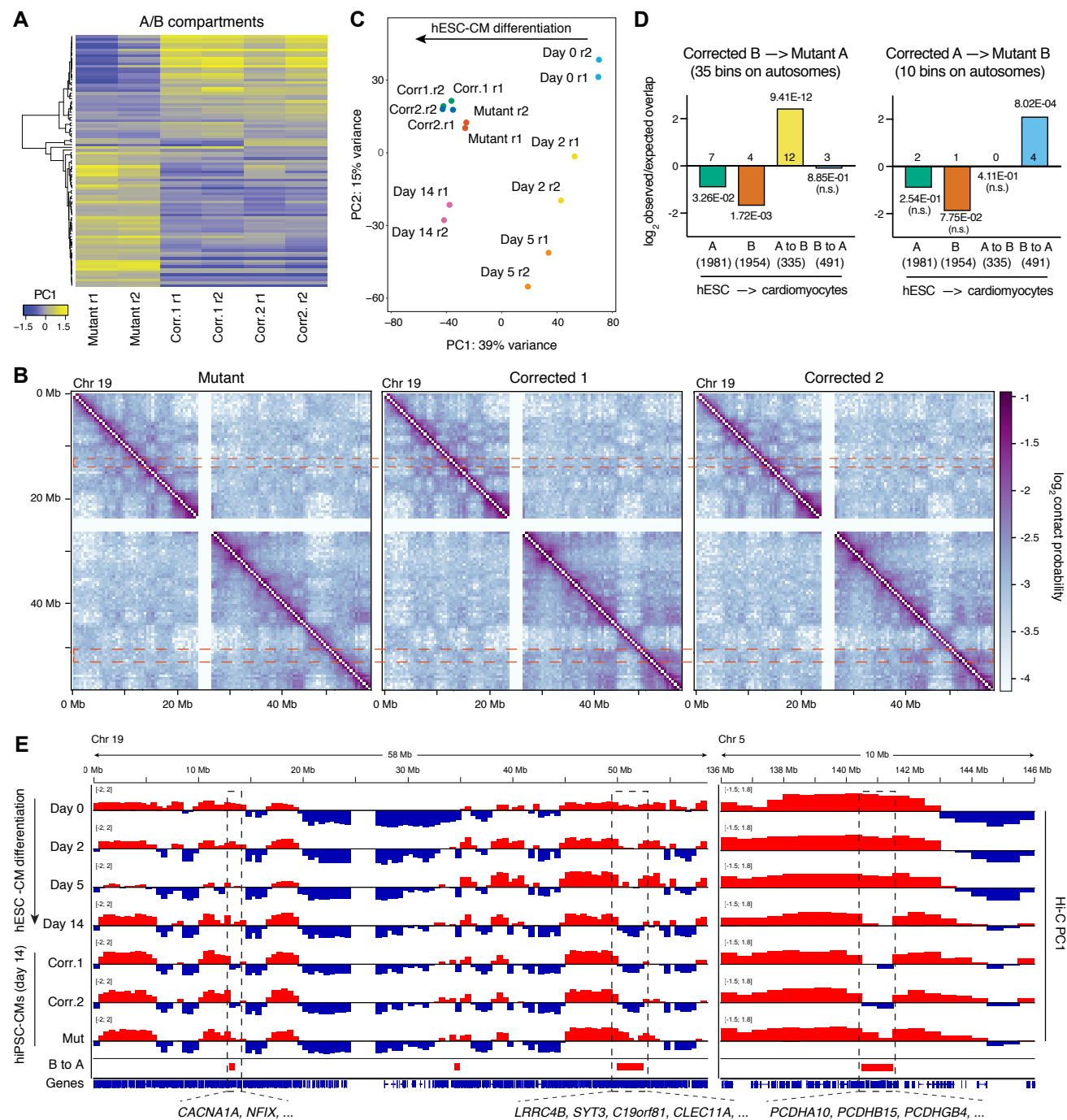
Figure 6. Chromatin compartment transitions in lamin A/C haploinsufficient hiPSC-CMs.

(**A**) Heatmap of all significantly different A/B compartment scores (Hi-C matrix PC1; $p < 0.05$ by one-way ANOVA; n = 2 differentiations; Table S4) in 500 Kb bins that changed PC1 sign between two or more conditions. Positive and negative PC1 indicate A and B compartmentalization, respectively. (**B**) Representative log-transformed contact probability maps for chromosome 19. Topologically associating domains (TADs) are visible as squares along the diagonal. TADs within the same compartment interact off the diagonal as indicated by the symmetrical checkerboard

47

1497   patterns. Two genomic regions which show different compartmentalization in mutant hiPSC-CMs are indicated by

1498   dashed boxes to highlight the differences in contact probabilities with other genomic regions off the diagonal. (**C**)

1499   Linear dimensionality reduction by principal component analysis of A/B compartment scores from Hi-C data of

1500   mutant and corrected hiPSC-CMs, and hESC-CMs sampled at different time points of differentiation (Fields et al.,

1501   2017). The amount of variance captured by each of the two main principal components (PC) is reported, and the

1502   biological interpretation for the PC1 axis is indicated. (**D**) Significance of the overlap between changes in A/B

1503   compartments in mutant hiPSC-CMs and those occourring during hESC-CM differentiation. The number of genomic

1504   bins within each of the categories is indicated, and p-values were calculated by chi-squared tests. Note that only

1505   autosomes were considered. (**E**) Representative genomic tracks of chromatin compartmentalization for

1506   chromosome 19 and a section of chromosome 5. Positive and negative Hi-C matrix PC1 scores are shown in red

1507   and blue, and indicate 500 Kb genomic bins in the A and B compartments, respectively. Genomic regions that

1508   transition from A to B during hESC-CM differentiation but remain in A in mutant hiPSC-CMs (noted as B to A) are

1509   indicated by dashed boxes. Selected genes found within such regions are listed (refer to Fig. 7 and Fig. S4).

47
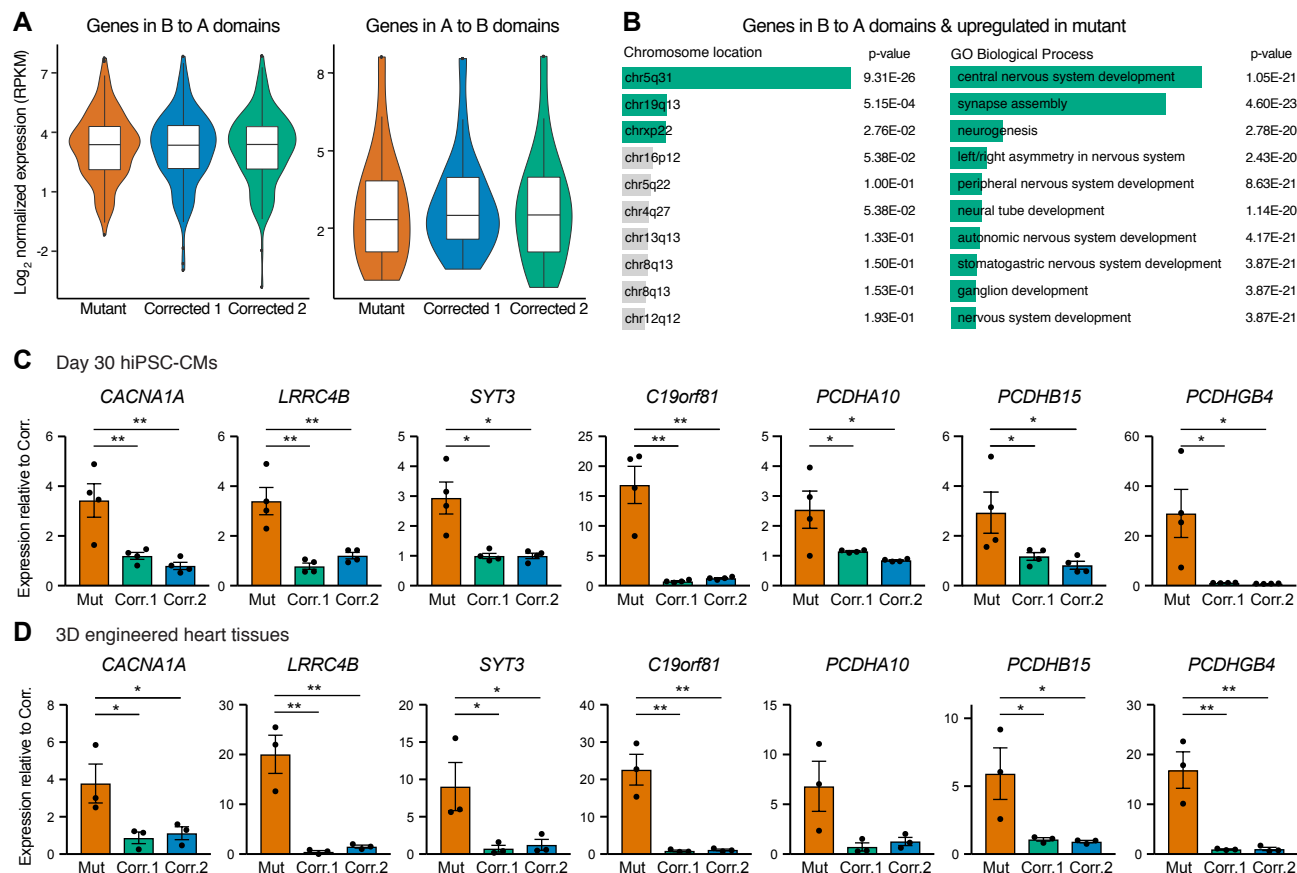
Figure 7. Correlation between altered chromatin compartmentalization and gene expression changes in lamin A/C haploinsufficient hiPSC-CMs.

(**A**) Violin plots showing the expression of genes found with lamin A/C-sensitive domains (average expression in RNA-seq data from 3 differentiations). Boxplots indicate the first quartile, median, and third quartile, while whiskers are from the 5th to 95th percentile. In the left panel, note that the tail of genes expressed at very low levels in corrected hiPSC-CMs is less pronounced in mutant cells. (**B**) Selected results from ontology enrichment analyses of upregulated genes in domains aberrantly found in the A compartment in mutant hiPSC-CMs (average fold-change > 2; Fig. S3C). Term as are listed by their rank based on the combined score, and the p-values are reported (Table S5). (**C-D**) RT-qPCR validation of gene expression changes in hiPSC-CMs matured by culture *in vitro* for 30 days (C) or by generation of 3D-EHTs (D). Differences *versus* mutant were calculated by one-way ANOVA with post-hoc Holm-Sidak binary comparisons (* = p < 0.05, ** = p < 0.01; n = 4 differentiations for panel C, and n = 3 3D-EHT batches for panel D; average ± SEM).

48

1523
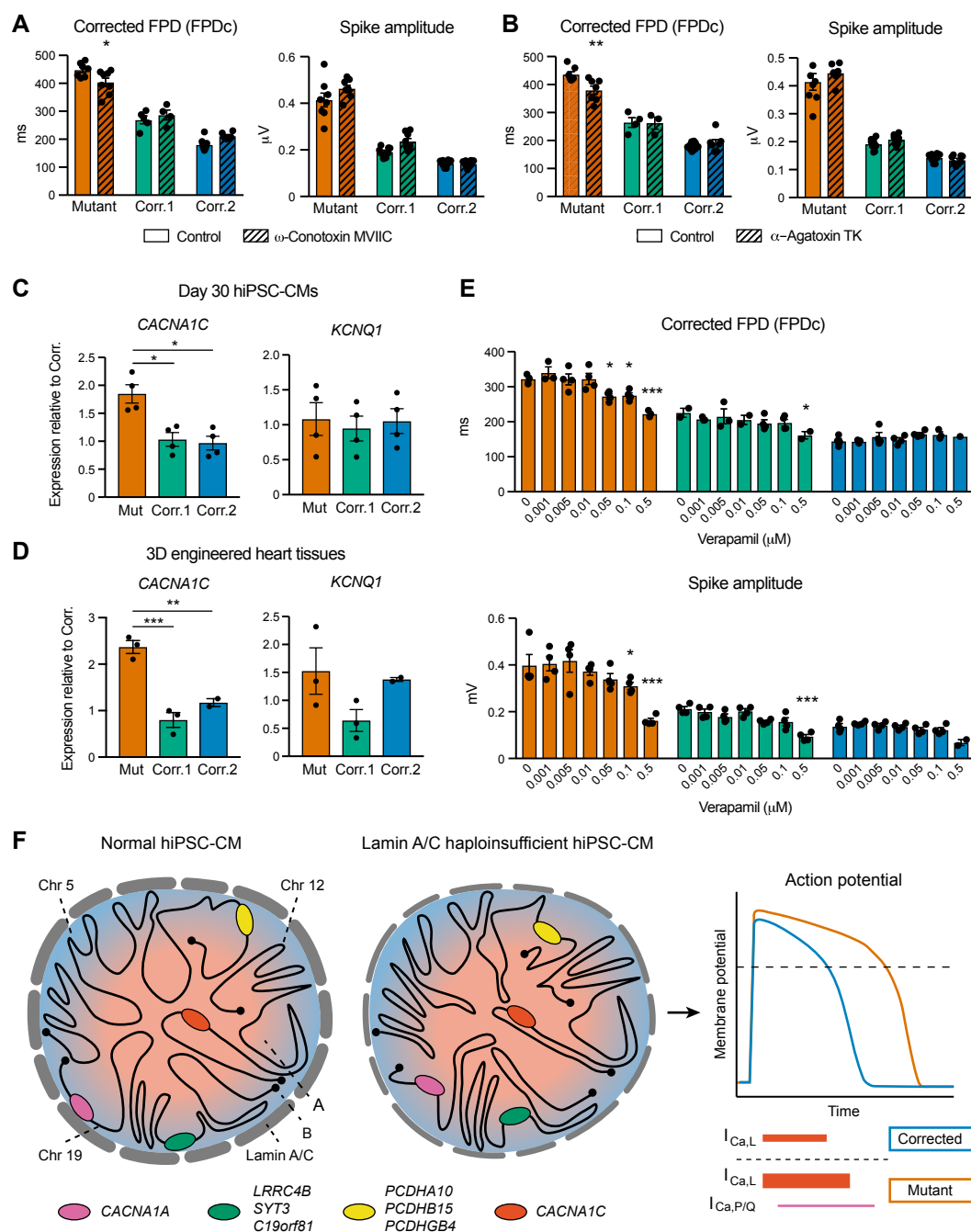
Figure 8. Role of P/Q- and L-type calcium currents in electrophysiological abnormalities of lamin A/C haploinsufficient hiPSC-CMs.

(**A-B**) Representative quantifications of electrophysiological properties from MEA analyses. hiPSC-CMs were maintained in standard culture conditions, or pre-treated for 20 min with the indicated inhibitors for P/Q-type calcium channels (ω-Conotoxin MVIIC: 2 μM; ω-Agatoxin TK: 0.5 μM). Differences *versus* mutant were calculated by one-way ANOVA with post-hoc Holm-Sidak binary comparisons (* = $p < 0.05$, n = 3-8 wells; average ± SEM). (**C-D**) RT-qPCR validation of gene expression changes in hiPSC-CMs matured by culture *in vitro* for 30 days (C) or by

1531   generation of 3D-EHTs (D). Differences *versus* mutant were calculated by one-way ANOVA with post-hoc Holm-

1532   Sidak binary comparisons (* = $p < 0.05$, ** = $p < 0.01$, *** = $p < 0.001$; n = 4 differentiations for panel C, and n = 3

1533   3D-EHT batches for panel D; average ± SEM). (**E**) As in panels A-B, but hiPSC cm were pre-treated for 10 min with

1534   increasing doses of the L-type calcium channel blocker verapamil. (**F**) Proposed model for the chromatin

1535   compartmentalization-dependent and independent effects of lamin A/C haploinsufficieny in developing hiPSC-CMs.

1536   Mutant cells have stronger interactions within the A compartment and decreased intermixing of A and B

1537   compartments. *Trans* interactions are globally reduced, while large chromosomes (exemplified by chromosomes 5

1538   and 12) and small-chromosomes (exemplified by chromosome 19) self-associate more. Compartmentalization of

1539   selected genomic hotspots is dysregulated, in particular for compartments that developmentally transition from A to

1540   B in normal hiPSC-CMs but remain in A in mutant cells (exemplified by the magenta, green, and yellow loci). A

1541   large number of genes are dysregulated independently of chromatin compartment changes (exemplified by the red

1542   locus). These combined effects drive stronger L-type calcium currents (thick red line) and ectopic P/Q type calcium

1543   currents (thin magenta line), leading to prolonged action potentials, stronger calcium fluxes, systolic hyperfunction,

1544   and diastolic dysfunction.